



Cite this: *CrystEngComm*, 2017, 19, 2144

Received 16th February 2017,
Accepted 6th March 2017

DOI: 10.1039/c7ce00322f

rsc.li/crystengcomm

Crystal engineering for novel functionalities with oxide thin film epitaxy

Daichi Oka^a and Tomoteru Fukumura^{*ab}

Oxides have become recognized as one of the most promising next-generation electronic materials due to the varieties of rich functionalities such as superconductivity, ferromagnetism, ferroelectricity, transparency, etc. In addition to the great diversity of functionalities, oxygen affinity with many other elements provides opportunities for crystal engineering in oxides: the properties can be tuned by modification of the bonding state of oxide ions. Epitaxy has been used as a powerful method to conduct such crystal engineering on oxides in the form of thin films. We give a review of recent advancements related with crystal engineering of oxide thin films *via* epitaxy techniques that control the microscopic crystallographic environment.

1 Introduction

Over the long period of human history, oxides have been used as structural materials, insulators, and ceramics because of their superior stability in air. In this half century, their versatile functionalities have been unveiled, such as transparency, electric/ionic conductivity, ferroelectricity, ferromagnetism, multiferroicity, and superconductivity, all of which could contribute to key functions in next generation devices.^{1–8} In contrast with established semiconductors such as Si and III–V compounds, oxides possess a large number of chemical compositions and crystal structures owing to the extraordinary affinity of oxygen to many elements. The oxygen affinity also enables the formation of various kinds of atomic coordination networks *via* oxygen ions, providing the possibility of combining various functionalities and constructing future devices beyond silicon-based technology.⁹ Accordingly, “crystal engineering” is useful to control properties of oxides by changing the microscopic crystallographic environment as described in this article.

In the initial period of oxide electronics, oxides have been investigated as ceramic materials mainly in the form of bulk powders, sintered pellets, and polycrystalline films on demand of the traditional ceramic industry. Such oxides are usually the most stable phases due to the mostly thermodynamic equilibrium processes. Since the discovery of high- T_c superconductivity in layered cuprates,¹⁰ the significant progress of thin film epitaxy techniques of oxides has boosted oxide electronics. For example, high quality epitaxial thin films

are indispensable for the fabrication of heteroepitaxial structures such as the Josephson junction.¹¹ In addition, such epitaxy techniques are useful not only for thin film growth of existing functional oxides but also for thin film synthesis of new compounds and metastable phases *via* crystal engineering of oxides.^{12–14}

At the initial stage of epitaxial growth, a single crystalline substrate serves as a seed for thin film crystallization. The initially deposited thin film becomes a self-seed for the subsequently deposited thin film, and eventually a complete epitaxial thin film is deposited. Single crystalline substrates stabilize various metastable structures owing to the epitaxial force, yielding novel functionalities. Such behaviour has already been recognized in the cases of Si and III–V semiconductors. However, more ionic oxides seem to be more attractive to tailor various structures and functionalities *via* crystal engineering using thin film epitaxy.

In this review article, we provide an overview of the recent progress in thin film epitaxy of homogeneously structured oxides as a convenient tool to create rich functionalities through chemical design. In section 2, representative film

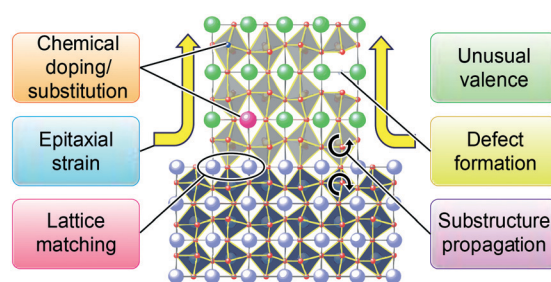


Fig. 1 Schematic diagram of a perovskite heterostructure with compressive strain showing the possible influence of epitaxy on thin films.

^a Department of Chemistry, Graduate School of Science, Tohoku University, Sendai 980-8578, Japan. E-mail: tomoteru.fukumura.e4@tohoku.ac.jp

^b WPI Advanced Institute for Materials Research, Tohoku University, Sendai 980-8577, Japan

growth techniques are introduced. In section 3, successful examples of crystal engineering of oxides are described, as schematically shown in Fig. 1. This review article does not intend to cover all fields and pioneering works of oxide epitaxial thin films. A detailed insight into the heteroepitaxy of nonisostructural complex oxides has been recently reviewed by Wong *et al.*¹⁵ Extensively studied oxide heterointerfaces, heterostructures, and self-assembled structures are discussed elsewhere.^{16–19}

2 Film growth techniques

Various techniques of oxide thin film epitaxy have been developed so far (Table 1). Pulsed laser deposition (PLD), sputtering deposition, and molecular beam epitaxy (MBE) are classified as physical vapour deposition methods, in which atomic, molecular, and/or ionic chemical species are physically evaporated by means of laser irradiation, ion bombardment, and thermal heating, respectively. These highly established and easy-to-use techniques are widely used because of the availability of high quality thin films. On the other hand, chemical vapour deposition (CVD) and some

solution-based methods are cost-effective and easy-to-modify processes. Also, novel deposition techniques such as hybrid MBE, atomic layer deposition (ALD), and mist CVD have been developed for scientific and industrial studies.

Growth mechanism and phase stability depend on each technique. In gaseous phase processes, the oxidation state of the thin film can be tuned by proper supply of gases such as oxygen and ozone. In solution processes, the oxidation state can be tuned by oxidizers and reductants. The kinetic energy of the deposited species is an important factor.²⁰ The kinetic energy in the case of thermal evaporation techniques such as MBE and CVD is as small as ~ 0.1 eV, often resulting in formation of the most stable phase with less intrinsic chemical vacancies in crystals. In contrast, sputtering deposition and PLD generate species with a high kinetic energy of several eV for the deposition of oxides. The deposited species such as atoms and molecular clusters are sometimes trapped at a local minimum state in the energy landscape rather than the global minimum state owing to the high kinetic energy; thus metastable phases are sometimes formed. Also in the case of low temperature thermal processes such as ALD and topotactic reactions, metastable phases are sometimes

Table 1 Typical growth conditions and advantages/disadvantages of representative epitaxial thin film growth methods. OP, BP and AP stand for operation pressure, base pressure, and atmospheric pressure, respectively

Methods	Sources	Supply	Atmosphere	Pressure (Pa)	Particle energy (eV)	Temperature (°C)	Advantage	Disadvantage
Pulsed laser deposition	Sintered ceramics/single crystals	Laser ablation	Vacuum, O ₂ , Ar, H ₂ , N ₂ , or mixtures	OP: 10 ⁻⁷ –10 ⁻⁶ BP: 10 ⁻⁷ –10 ⁻⁶	1–100	500–1200	<ul style="list-style-type: none"> Stoichiometric transfer Wide applicability 	<ul style="list-style-type: none"> Low growth rate Spontaneous defect formation
Sputtering	Sintered ceramics/metal plates	Sputtering	Ar, Ne, Kr, Xe, O ₂ , H ₂ , N ₂ or mixtures	OP: 10 ⁻² –10 ⁻³ BP: 10 ⁻⁶ –10 ⁻³	1–10	500–800	<ul style="list-style-type: none"> High growth rate Large area 	<ul style="list-style-type: none"> Damage by ionized particle Elemental selective supply rate
Molecular beam epitaxy	Elemental substances/metal organics	Thermal evaporation	Vacuum, O ₂ or O ₃	OP: 10 ⁻⁵ BP: 10 ⁻⁸ –10 ⁻⁷	0.1–1	500–1200	<ul style="list-style-type: none"> Easy control of supply ratio of elements Precise stoichiometry (hybrid MBE) 	<ul style="list-style-type: none"> Low growth rate Fixed target
Chemical vapour deposition	Metal organics/hydride/halide	Thermal evaporation and gas flow	H ₂ , N ₂ , O ₂ , O ₃ , H ₂ O or mixtures	100–AP	0.1–1	100–800	<ul style="list-style-type: none"> Easy control of composition 	<ul style="list-style-type: none"> Low crystallinity Limitation of precursor (vapour pressure)
Atomic layer deposition	Metal organics	Thermal evaporation of precursor molecules	O ₂ , O ₃ , N ₂	100–AP	0.1–1	200–400	<ul style="list-style-type: none"> Flat even on textured surface Large area 	<ul style="list-style-type: none"> Fixed target
Solution route	Precursors soluble in solvents	Direct supply of precursor solutions	Atmospheric or controlled conditions	AP	—	500–1000	<ul style="list-style-type: none"> Easy setup Large area 	<ul style="list-style-type: none"> Low crystallinity
Mist chemical vapour deposition	Precursors soluble in solvents	Gas flow of precursor solution mist	O ₂ , O ₃ , N ₂	AP	—	500–1000	<ul style="list-style-type: none"> Easy setup Large area 	<ul style="list-style-type: none"> Limitation of pressure
Solid phase epitaxy	—	—	Atmospheric or controlled conditions	10 ⁻⁷ –AP	—	500–1200	<ul style="list-style-type: none"> Flexible control of conditions 	<ul style="list-style-type: none"> Highly material dependent

obtained because of the reaction not attaining the global minimum. In this section, the basic principles of film synthetic methods and recent advances are described from the viewpoint of crystal engineering.

2.1 Pulsed laser deposition

The main components of PLD are a precursor target and a substrate usually placed face-to-face with each other in a vacuum chamber and a high power laser for ablation of the target (Fig. 2a).^{21,22} The target is typically a sintered ceramic pellet or a single crystal of oxides, and its composition is the same as that of the films because of usually unchanged transfer of the composition during deposition as described below. A short wavelength is generally preferable in the case of oxides because negligible particles are generated on the film due to the short penetration depth of laser light. The most commonly used lasers are the Nd:Y₃Al₅O₁₂ (Nd:YAG) solid state laser with a harmonic wavelength λ between 255 and 1064 nm and ultraviolet excimer gas lasers such as KrF ($\lambda = 248$ nm), XeCl ($\lambda = 308$ nm), and ArF ($\lambda = 157$ nm). Excimer lasers possess higher energy stability in the ultraviolet region, and hence are appropriate to deposit flat and dense films of oxides. The atmospheric conditions inside the chamber are highly flexible depending on the film compounds: various gases such as O₂, N₂, H₂, Ar, NO₂, *etc.* can be used at a wide range of pressures from 0 to ~ 100 Pa. The ablation process with a nanosecond scale duration, ~ 5 ns and ~ 20 ns for Nd:YAG and excimer lasers, respectively, consists of complicated multiple steps despite a seemingly simple process.²³ When a target is ablated by a laser pulse, the target surface is locally

heated up rapidly within the picosecond scale to melt and then evaporate. The ejecta, so-called plume, absorbs the laser pulse to promote plasma formation including electrons, ions, molecular clusters, and so on. Subsequently, the adiabatically expanded plume is propagated normal to the target surface on the substrate, resulting in film deposition. The directional and instantaneous propagation of the plume contributes to an approximately complete transfer of the chemical composition from the target to the film, which is a considerable advantage of PLD. This is the case especially when the atmosphere is under high vacuum, in which collision between the ejected species and the existing gaseous molecules is negligible²⁴ though the transfer of stoichiometric composition is not always ideal as described in section 3. Because of the high kinetic energy of the chemical species in plume under high vacuum, the PLD process is highly non-equilibrium, sometimes leading to the formation of metastable phases.

PLD chambers are generally equipped with a substrate heater for high temperature deposition. A halogen lamp surrounded by a gold mirror has been widely used for the heater. Today, infrared continuous solid state lasers such as the Nd:YAG laser, which was originally used as a steel cutter, are available for higher temperature and rapid heating and cooling.²⁵ The substrate temperature quickly exceeds over 1000 °C. Also, reduction of the laser spot size is useful to make a temperature gradient within a 1 cm-sized substrate, enabling rapid optimization of growth temperature.²⁶ Such efficient optimization of growth parameters was attempted also for film composition by using a combinatorial approach.²⁷ Here, the system is equipped with a combination of automatic moving masks and a target exchanger, in which

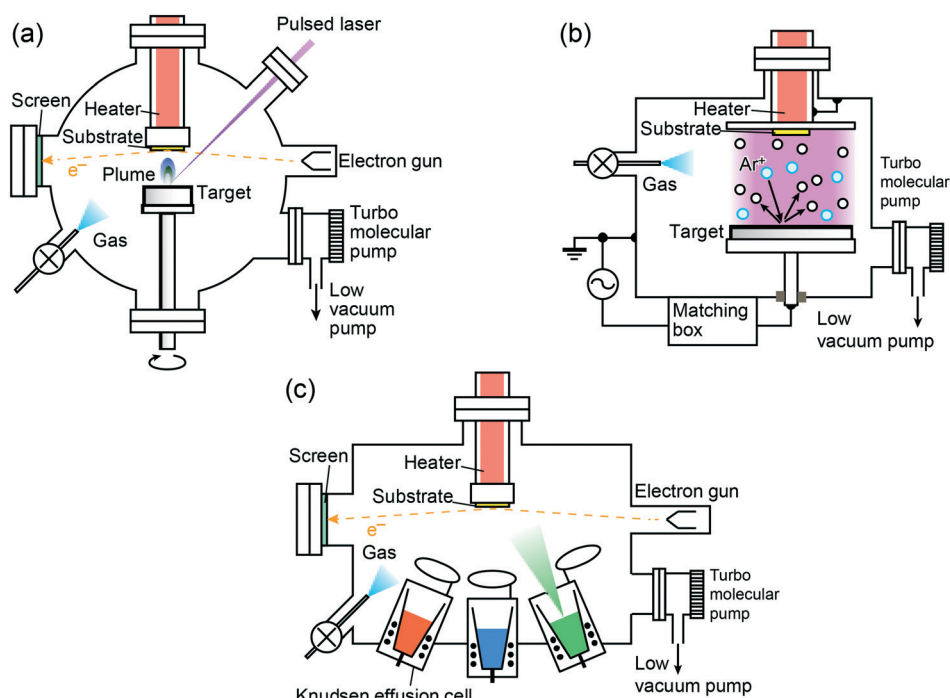


Fig. 2 Typical setups of physical vapour deposition. (a) Pulsed laser deposition, (b) rf sputtering deposition, and (c) molecular beam epitaxy.

a combinatorial thin film library with discrete phases and composition-spread phases can be manufactured on a single substrate.

In situ monitoring of the film structure during growth is applied for efficient optimization of growth conditions and understanding of film growth mechanisms by using reflection high energy electron diffraction (RHEED). An electron beam arriving at the sample surface with a shallow incident angle is reflected and probed on a photoluminescence detector screen placed at the opposite side of the electron gun as a diffraction pattern (Fig. 2a). Because of the small penetration depth of the electron beam, the diffraction pattern reflects the crystal structure and morphology of the topmost surface of the film. The temporal change of diffraction intensity during deposition corresponds to the surface coverage and growth mode of molecular layers.²⁸ Hence, the deposition of a superlattice can be conducted.²⁹ By using the combinatorial approach, parallel synthesis of superlattices with different sequences is possible.³⁰

2.2 Sputtering deposition

Sputtering deposition is one of the most frequently used film growth methods especially in industrial applications due to its large areal deposition with a high growth rate.^{31,32} The chamber is filled generally with inert gases such as noble gases and N₂ with a pressure of around 1–10 Pa. For deposition of films, the electrical bias between an anode beneath the target and a cathode attached to the substrates accelerates positively ionized atoms of the process gas up to a kinetic energy of 0.1–10 keV, which impinge on the target surface on the anode, invoking a glow discharge with a relatively high current density.³³ The ejected particles lose their kinetic energy significantly by collision with the high pressure gas molecules before reaching the substrate surface.

For sputtering of insulators, high frequency rf voltage (typically 13.56 MHz) is applied, while dc voltage is used for conductors such as metals (Fig. 2b). Recently, magnetrons were often attached to the backside of targets for capturing secondary electrons from the target surface, in order to increase the yield rate of ejected atoms and to prevent sputtering damage of the film surface by the electrons. Reactive sputtering is also used to deposit oxide films by oxidizing metal species from the target under O₂ gas during deposition, in which a dc voltage source is often used and is cost effective in spite of a lower deposition rate than that of rf sputtering.

A high kinetic energy of about 1 keV of incident ions required for a sufficient yield rate over unity (knock-on mode) tends to degrade film quality by generating defects such as grain boundaries and gas implantation. Hence, reduction of gas pressure has been attempted by several methods such as collimation of ions, gas ionization with rf induced plasma, and ion beam assisted deposition.³⁴ Because of the different sputtering rate for each element and the multiple scattering of the ejected particles, stoichiometric transfer like the PLD process is usually difficult. Accordingly, binary oxides are the

major target for the sputtering method, though precise optimization of deposition conditions enables the deposition of complex oxides and even their superlattices.^{35,36}

2.3 Molecular beam epitaxy

MBE is a film growth method based on the straightforward concept of supplying each constituent atom of the objective material in an appropriate ratio. The constituent atoms are supplied on the substrate separately from Knudsen effusion cells under ultrahigh vacuum conditions (Fig. 2c).³⁷ Oxygen is usually supplied from O₂, O₃, or O radical gases. Recently, a quite small MBE chamber, less than 1 m³ in volume, has been developed, enabling sample transfer *in vacuo* to vacuum measurement systems such as a synchrotron beam line,³⁸ similar to a small PLD chamber.³⁹

Compared to PLD and sputtering, the MBE process supplies highly pure constituent elements with much smaller kinetic energy due to the thermal evaporation characteristics, usually realizing an almost thermal equilibrium condition. Thus, the resultant phase diagram is almost governed by thermodynamics.^{40,41} If the composition is properly tuned, highly stoichiometric and pure thin films of binary oxides can be deposited, as demonstrated by *e.g.* a fractional quantum Hall effect in the Mg_{0.05}Zn_{0.95}O/ZnO heterostructure.⁴²

In the case of complex oxides, off-stoichiometry often happens because of a poorer desorption process due to the ionic nature of oxides. A breakthrough was achieved by the development of a technique called “hybrid MBE”, in which MBE and high vacuum CVD are combined.⁴³ In this method organic metal is used as a precursor, which desorbs from the film in case of excess composition. Son *et al.* reported the highest electron mobility over 30 000 cm² V⁻¹ s⁻¹ in La-doped SrTiO₃ epitaxial thin film deposited from Sr, La, oxygen plasma, and titanium tetraisopropoxide precursors.⁴⁴ Matsubara *et al.* observed a quantum Hall effect in a δ -doped STO epitaxial thin film deposited using hybrid MBE.⁴⁵ These results are indicative of the successful growth of ideally stoichiometric and very high quality films.

2.4 Chemical vapour deposition

Chemical vapour deposition (CVD) using chemical reactions during deposition is categorized as a counterpart of physical vapour deposition techniques. CVD includes various relatives such as plasma CVD, low pressure CVD, and metal–organic CVD. These CVD processes are suitable for industrial applications because of high operation pressures from low vacuum to atmospheric pressure.

CVD consists of three main processes: transfer of precursor molecules, chemical reactions at the substrate, and removal of by-products.³¹ Firstly, thermally evaporated precursors are transferred to the reactor by gas flow. Then, the precursors are in part adsorbed and decomposed into the objective solid phase and by-products on heated substrates in the reactor. The by-products, designed to have a higher vapour pressure, are desorbed from the substrate, yielding the objective material

films. Compared to the homogeneous decomposition reaction of precursors in the gas phase prior to deposition on the substrate, the heterogeneous reaction of precursors on the substrate surface is preferable to deposit a dense and smooth film strongly bonded with the substrate.⁴⁶ For the decomposition of precursors, plasma and light including laser can be used instead of heat, sometimes causing uncontrollable chemical reactions.⁴⁷ Haga *et al.* succeeded in synthesizing high quality epitaxial thin films of ZnO by controlling the reactivity between $\text{Zn}(\text{C}_2\text{H}_5)_2$ and CO_2 with plasma.⁴⁸ CVD processes under high vacuum conditions are also useful to synthesize unstable compounds under high pressure. In such processes, precursor species are supplied to the substrate as a molecular beam without collision like in MBE, and individual decomposition of each supplied molecule takes place.⁴⁹ High vacuum CVD used for a Al_2O_3 film⁵⁰ was later applied to high- T_C superconductor thin films such as $\text{YBa}_2\text{Cu}_3\text{O}_{7-x}$ (ref. 51) and $\text{LaBa}_2\text{Cu}_3\text{O}_{7-x}$.⁵² CVD combined with MBE was used for complex oxide thin films as described above.

2.5 Atomic layer deposition

ALD is an emerging technique to obtain highly flat and homogeneous films, categorized as a CVD process. Layer-by-layer self-limiting chemical reactions of organic precursors enable obtaining homogeneous films on various surfaces including nanostructures with a high aspect ratio.^{53,54} ALD can be conducted under low vacuum and low temperature, thus it is applied for various applications such as flat panel displays. For example, binary oxide AO_x films are deposited in the following sequence (Fig. 3). Metal organic precursors supplied with inert gas are adsorbed on the bare substrate surface to form a single molecular layer with full coverage, and unreacted precursors and by-products are removed with inert gas by purging the chamber. Next, the layer was fully oxidized to form AO_x by introducing co-reactants such as H_2O and O_3 , followed by purging to remove redundant co-reactants and by-products. By repeating these cycles, a thin film of AO_x is deposited in a layer-by-layer manner. For the deposition of complex oxides, the corresponding molecular layers are deposited alternately (*e.g.* AO and BO_2 layers to form perovskite ABO_3), resulting in difficult control of stoichiometry in ternary and quaternary oxides.⁵⁵

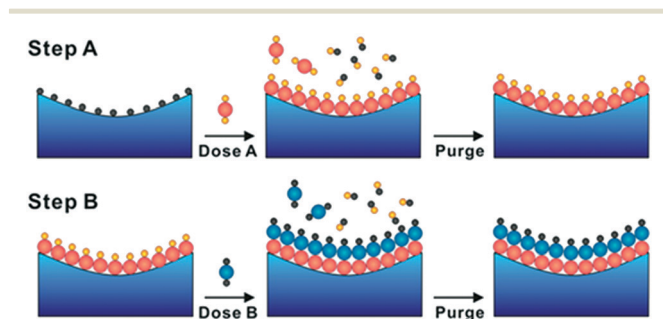


Fig. 3 Depositing sequence of binary material using atomic layer deposition. Reproduced with permission from ref. 53. Copyright 2013, American Chemical Society.

Recently, appropriate precursors were developed to obtain epitaxial thin films of ternary oxides. For example, Coll *et al.* reported the direct growth of spinel Co_2FeO_4 epitaxial thin films on the (100) and (110) planes of STO substrates at a low temperature of 250 °C.⁵⁶ In this case, the Co-rich spinel pure phase was obtained as a fully relaxed film, exhibiting isotropic ferromagnetic behaviour down to 10 nm thick. Emery *et al.* reported the epitaxial growth of Sn doped In_2O_3 on the (100), (110), and (111) planes of YSZ substrate also at a low temperature of 250 °C.⁵⁷ Excellent coherent growth on the substrate was seen in contrast with the case of the spinel films despite the lack of an atomically flat surface like MBE and PLD deposited films.

2.6 Solution process

One of the most frequently used solution processes in oxide film growth is the sol-gel method. In this method, precursor gels are prepared by dissolving metal compounds such as alkoxides into solvents, followed by hydrolysis and gelation reactions at a mild temperature of <100 °C.⁵⁸ These gels are dip- or spin-cast on substrate homogeneously and are crystallized by calcination. During the gelation process, the component elements are homogeneously mixed at an atomic level in contrast to the vapour phase reactions, where the distribution of adsorbed atoms/molecules is predominated by kinetics, so that the film is formed almost in an equilibrium state. The easy processing is useful for practical applications, although there are several concerns such as the toxicity of organic solvents and precursors, insufficient growth rate, and poor film quality. Zhao *et al.* recently developed a fast growth route of $\text{YBa}_2\text{Cu}_3\text{O}_{7-\delta}$ epitaxial thin films using a nontoxic propionate-based solution.⁵⁹ The obtained film showed superconducting behaviour with a critical current density as high as 3.7 MA cm^{-2} at 77 K. Also, a technique called prompt inorganic condensation (PIC) is being studied extensively.⁶⁰ In PIC, environmentally friendly aqueous solutions of metal nitrates are used as precursors in order to obtain high quality films.

The solution process is suitable for complex oxides with multiplex crystallographic blocks due to its quasi-equilibrium nature. For example, Rivas-Murias *et al.* reported the successful synthesis of epitaxial thin films of misfit cobaltates ($[\text{AO}]_m[\text{CoO}_2]$) ($A = \text{Bi}, \text{Ba}, \text{Sr}, \text{Ca}, \text{Co}$) by sintering spin-coated aqueous solutions including polyethyleneimine.⁶¹ The polyethyleneimine decomposed at a slightly lower temperature than crystallization, preventing undesirable reactions, resulting in a clear epitaxial interface with LAO substrates. The cobaltates are composed of periodically stacked insulating rock salt [AO] layers and electrically conducting edge-sharing CoO_6 octahedral layers, exhibiting bulk-like p-type electrical conduction and good thermoelectric properties. It is noted that epitaxial thin film deposition of the cobaltates was difficult by using physical vapour deposition techniques due to the interfacial amorphous layer probably formed by their non-equilibrium nature.⁶²

2.7 Mist CVD

Mist CVD is a solution based technique developed recently (Fig. 4).^{63,64} A solution of precursors in a supply unit is converted into mist particles whose diameters are 2–3 μm using an ultrasonic transducer. The mist is diluted and transferred by carrier gas on the substrate in a reaction unit. Because of the simple setup operated under atmospheric pressure, the system is highly cost-effective. In addition, a high vapour pressure of precursors is unnecessary. The only requirement for precursors is solubility in solvents, which is not a difficult problem.

The epitaxial growth of various binary oxides such as ZnO, Ga₂O₃, Al₂O₃ and In₂O₃ has been demonstrated.⁶⁴ Despite the ambient growth conditions, these films showed high crystallinity with a narrow full width at half maximum (FWHM) of the rocking-curve, less than 0.01°, comparable to that of the vacuum processes.⁶⁵ As a result, various thin films of mixed crystals and heterostructures have been deposited.⁶⁴ Recent studies were extended to epitaxial thin film growth of ternary oxides such as bismuth iron and yttrium aluminium garnets.^{66,67}

2.8 Topotactic reaction

A topotactic reaction is a post-deposition treatment to incorporate or remove elements while maintaining the crystal framework of mother compounds.⁶⁸ Light ions with low electric charge such as H⁺, H⁻, Li⁺, O²⁻ and F⁻ are often used in topotactic reactions because of their high ionic conductivity. For topotactic reactions of oxides, gaseous, liquid, and solid reagents can be used. Though topotactic reactions can be conducted for both bulk and thin film specimens, the thin film specimen has an advantage due to the high speed and homogeneous reaction (Fig. 5).⁶⁹

Topotactic reactions are sometimes reversible. Zhang *et al.* reported that ordered oxygen vacancies in semiconducting rhombohedral SrCoO_{2.8} are easily compensated for by annealing in air to form metallic cubic perovskite SrCoO₃, and restored by further annealing in vacuum.⁷⁰ Yoshimatsu *et al.* succeeded in reversible control of the topotactic reaction of Li⁺ ions in LiTi₂O₄ epitaxial thin film as the anode in a Li-ion battery structure using an electrochemical method.⁷¹ The superconductivity of LiTi₂O₄ was suppressed by intercalating Li⁺ ions, whereas it was recovered by successively deintercalating Li⁺ ions.

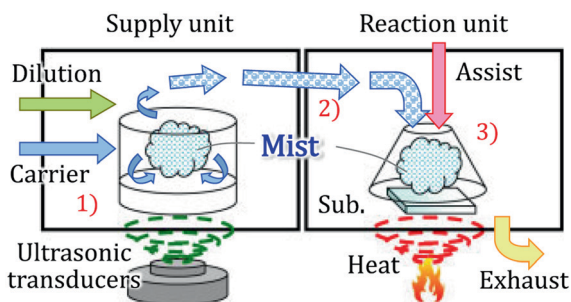


Fig. 4 Schematic setup of mist CVD. Reproduced with permission from ref. 63. Copyright 2014, The Japan Society of Applied Physics.

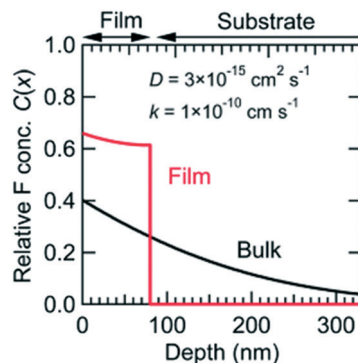


Fig. 5 Relative fluorine concentration ($C(x)$) vs. depth (x) curves after topotactic reaction, calculated for 80 nm thick thin film and bulk sample. The details are described elsewhere.⁶⁸ Reproduced with permission from ref. 69. Copyright 2014, The Royal Society of Chemistry.

3 Engineering of functionality

Lattice structures of epitaxial thin films are modulated by underlying substrates and/or epitaxially stacked adjacent layers (Fig. 1). Because the lattice structure significantly influences various physical properties of oxides, such structural modulations are useful to conduct engineering of functionality. For example, ferroelectricity in ionic crystals is sensitive to lattice modulation because lattice strain directly affects the polarization usually originating from atomic displacement.^{72,73} Structural engineering is also effective to control magnetism because of the crystal field splitting governed by lattice symmetry and the exchange coupling strongly depending on the bond length and tilt angle of M–O–M bonds (M: transition metal).⁷⁴

The bond length/angle and coordination state in a crystal unit can be varied *via* epitaxial growth, *i.e.* lattice distortion and polymorphism, respectively. It is possible to stabilize a coordination state of a metastable polymorph *via* lattice matching between film and substrate. Also, it is possible to maintain the mother compound structure even in the case of heavier impurity doping beyond its thermodynamic solubility limit, enabling very heavy doping in comparison with the bulk specimen. On the other hand, mismatch in lattice constants and/or symmetry between film and substrate causes strain in the film, resulting in lattice distortion under biaxial tensile/compressive strain, defect formation, and bond tilting. Such variations of bonding possibly cause a drastic change in the electronic structure and physical properties, especially when several electronic phases compete with each other. In this section, we will provide an overview of various examples of crystal engineering in oxide epitaxial films reported recently.

3.1 Metastable polymorphs

Increasing phase stability using lattice matching, called epitaxial force, is the basic idea in all studies of epitaxial growth. A polymorph is stabilized on specific substrates possessing a

similar structure. This approach has been widely applied to find novel metastable phases and to investigate structure dependent physical properties.⁷⁵

TiO₂ exhibits many functionalities by impurity doping and is one of the most extensively studied oxides that have many polymorphs: rutile, anatase, brookite, columbite, cotunnite, baddeleyite, and fluorite.⁷⁶ The rutile and anatase phases are the primary and secondary most stable phases under atmospheric conditions, respectively. The two stable polymorphs can be selectively formed on different substrates: the rutile phase on α -Al₂O₃ substrate and the anatase on lattice-matched perovskite substrates such as LAO and STO.^{76,77} Thus, their physical properties can be compared easily. For example, the anatase structure is more favourable to acquire both high transparency (over 95% at a wavelength of 600 nm) and low resistivity ($\sim 2 \times 10^{-4} \Omega \text{ cm}$ at room temperature) by Nb doping (Fig. 6).^{78,79}

Another example is the recently achieved growth of high quality α -Ga₂O₃ (corundum structure) epitaxial thin films by mist-CVD.⁸⁰ The α -phase is more attractive than the most stable β -phase from the viewpoint of functionality engineering, because of its capability to form a solid solution with other corundum oxides. For instance, wide range bandgap engineering from 3 to 9 eV is possible in solid solution with Al₂O₃ and In₂O₃, respectively.⁶⁴ (Al_xGa_{1-x})₂O₃ exhibited a linear variation of the bandgap between 5.3 and 8.8 eV, while (In_xGa_{1-x})₂O₃ showed a variation of the bandgap between 3.8 and 5.3 eV with bowing due to the relatively small miscibility between In₂O₃ and Ga₂O₃. Control of magnetism is also possible in α -Ga₂O₃ by mixing with magnetic corundum oxides such as Cr₂O₃ and Fe₂O₃, and (Ga_{0.42}Fe_{0.58})₂O₃ showed ferromagnetic properties at room temperature.⁸¹

The plane direction of the substrate can also be used to control the polymorphs. Lee *et al.* reported the selective growth of VO₂ polymorphs on perovskite oxide substrates (Fig. 7).⁸² Due to uniaxial or biaxial lattice matching between the film and the substrates in addition to their lattice symmetry, tetragonal VO₂ A-phase can be deposited on the (011)

planes of STO and LAO, but monoclinic B- and M1- phases on the (001) and (111) planes, respectively. The R-phase appears through phase transition from the M1-phase at high temperature. Because VO₂ shows largely varied physical properties such as electrical conductivity depending on the crystal structure (Fig. 7e), the selective growth of polymorphs is useful for their understanding and applications.

Epitaxial force can stabilize the metastable chemical composition, which otherwise results in phase separation. Lee *et al.* found a novel phase Sr₂Ti₇O₁₄ in a Ti-rich STO epitaxial thin film.⁸³ This metastable phase was obtained only in the case of a eutectic composition of 21 mol% SrO and 79 mol% TiO₂ on the (111) planes of perovskite oxides such as STO and (LaAlO₃)_{0.3}-(SrAl_{0.5}Ta_{0.5}O₃)_{0.7} (LSAT) at low growth temperature. Sr₂Ti₇O₁₄ is composed of local STO-like layers separated by TiO_x monolayers that have edge- and face-shared TiO₆ octahedra with mixed valence Ti³⁺ and Ti⁴⁺. The superexchange interaction between the Ti³⁺ sites resulted in an antiferromagnetic insulating characteristic. It is noted that the thermal conductivity was as low as 1.3 W mK similar to glasses, in which the low thermal conductivity was attributed to the significant interlayer phonon scattering and the low out-of-plane electrical conductivity.

3.2 Doping beyond solubility limit

Impurity doping is a fundamental way to tailor functionalities in semiconductors including oxides. The ionic charge and size of dopants significantly affect the physical properties of the mother compound. The amount of impurity doping has an upper limitation, *i.e.* solubility limit, over which phase separation or structural transition occurs, prohibiting heavier doping possibly connected with the emergence of novel physical properties. The epitaxial force extends the solubility limit while preserving the mother structure.

ZnO is an extensively investigated oxide semiconductor because of its promising potential for applications such as light emitting diodes (LEDs), photodetectors, and transparent transistors. To these ends, chemical doping is important to achieve p-type ZnO and bandgap engineering.^{84,85} For p-type doping, a wide range of dopants such as lithium, alkaline metals, copper, nitrogen, and phosphorus have been examined.⁸⁴ For bandgap engineering, the dopants were usually divalent ions such as Mg²⁺ and Cd²⁺, resulting in bandgap widening and narrowing, respectively. Here, the most stable phase of MgO and CdO is the rock salt structure, constraining their thermodynamic solubility limit in wurtzite ZnO to as low as <4% and <2%, respectively.⁸⁶ However, the solubility limits of MgO and CdO in ZnO were extended up to $\sim 50\%$ and $\sim 70\%$, respectively, by epitaxial stabilization of the wurtzite structure on α -Al₂O₃ (0001), ScAlMgO₄ (0001), and ZnO (0001), where the solubility limits depended on the growth method, conditions, and also the buffer layer.⁸⁷⁻⁹¹ The extended solubility resulted in a broad range of bandgap engineering ranging from 1.8 to 4.5 eV for wurtzite (Zn,Mg,Cd)O. Also, bandgap widening by alloying with wurtzite BeO whose bandgap is 10.6 eV has been suggested,⁹² and a

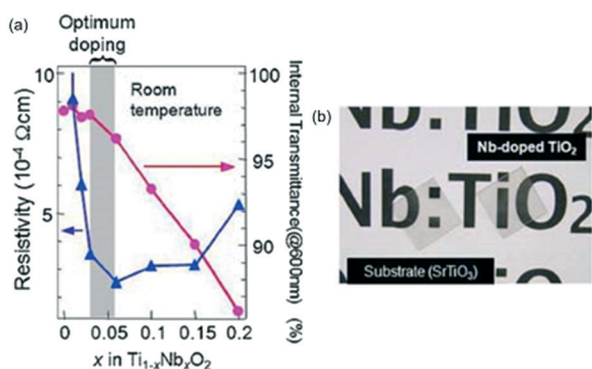


Fig. 6 (a) Resistivity and internal transmittance (at a wavelength of 600 nm) of Ti_{1-x}Nb_xO₂ epitaxial thin films. (b) A photograph of STO substrate (left) and Ti_{0.94}Nb_{0.06}O₂ epitaxial thin film on STO substrate (right). Reproduced with permission from ref. 79. Copyright 2010, WILEY-VCH.

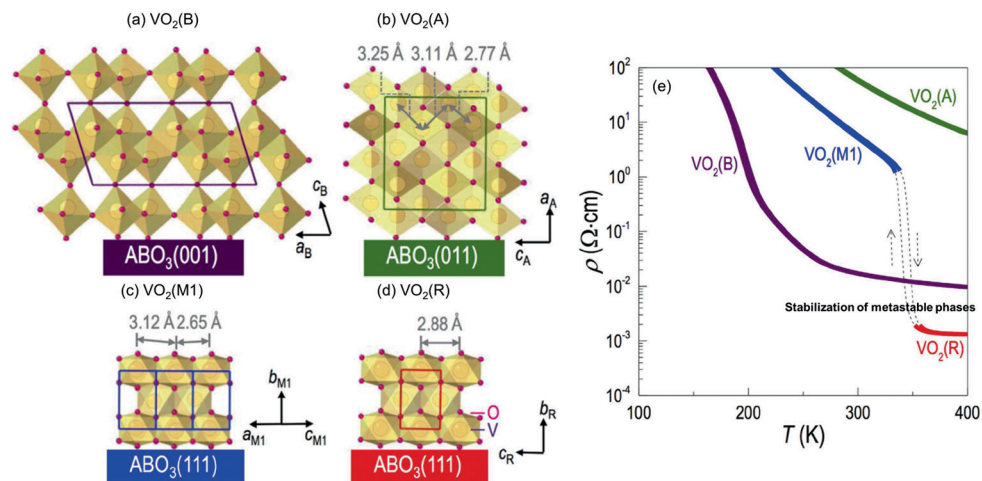


Fig. 7 Schematic crystal structures of (a) VO₂(B) on ABO₃(001), (b) VO₂(A) on ABO₃(011), (c) VO₂(M1), and (d) VO₂(R) on ABO₃(111) substrates. (e) Temperature dependence of resistivity for VO₂(B), VO₂(A), VO₂(M1), and VO₂(R) films. Reproduced with permission from ref. 82. Copyright 2016, Macmillan Publishers Limited.

Be_{0.08}Mg_{0.52}Zn_{0.40}O epitaxial thin film showed a bandgap of 5.11 eV.⁹³ The largely variable bandgap of doped ZnO is now applicable for barrier layers of quantum wells in LEDs, the semiconducting layer of Schottky photodetectors, the acceptor layer of solar cells, and so on.^{85,94,95}

Epitaxial stabilization of a doped semiconductor beyond the solubility limit of impurities sometimes leads to a new class of compounds, e.g. oxide-based diluted magnetic semi-

conductors such as transition metal doped ZnO, and a high temperature diluted ferromagnetic semitransparent semiconductor (Ti,Co)O₂ with anatase and rutile types, discovered using the combinatorial approach.^{96–98} (Ti,Co)O₂ shows a large magneto-optical effect in the ultraviolet-visible region and an anomalous Hall effect, and its magnetism can be controlled between paramagnetic and ferromagnetic states at room temperature by an electric field effect as well as

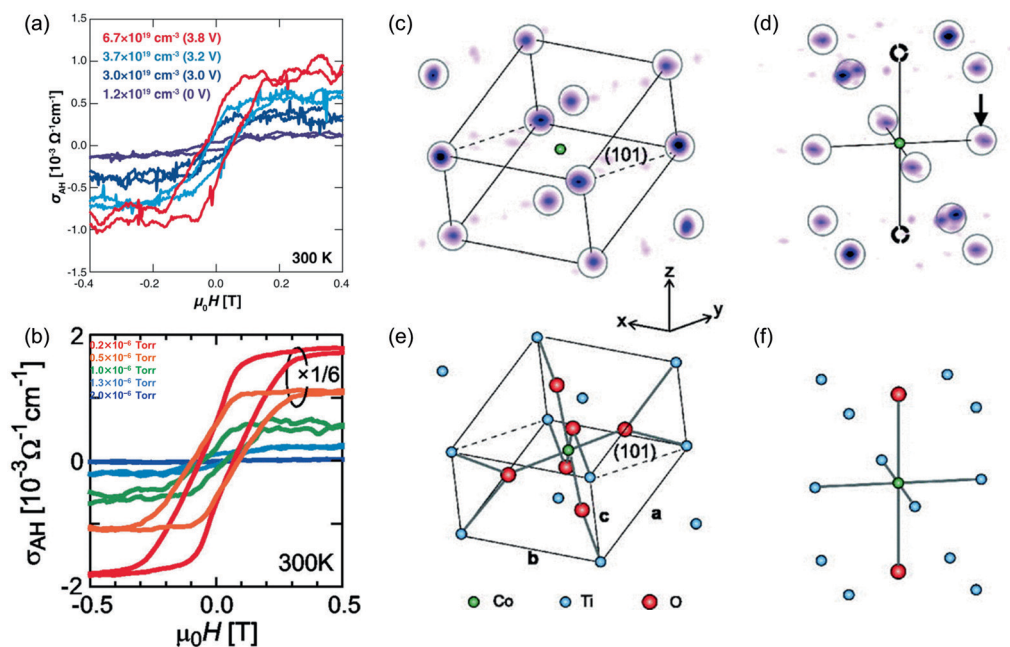


Fig. 8 (a) Magnetic-field dependence of the anomalous Hall conductivity σ_{AH} for anatase Ti_{0.90}Co_{0.10}O_{2- δ} films at 300 K, measured at different gate voltages (V_{G}) using an electric double layer transistor. The values of electron density n at each V_{G} are also shown. Reproduced with permission from ref. 100. Copyright © 2011 by the American Association for the Advancement of Science. (b) Anomalous Hall conductivity σ_{AH} at 300 K for anatase Ti_{0.90}Co_{0.10}O_{2- δ} films grown in various oxygen pressures. Reproduced with permission from ref. 99. Copyright © 2011 American Institute of Physics. (c and d) Real-space images around Co in (c) rutile Ti_{0.09}Co_{0.01}O₂ and (d) Ti_{0.95}Co_{0.05}O₂ films reconstructed from X-ray fluorescence holograms. (e and f) Structure models obtained from the images in (c) and (d), respectively. Reproduced with permission from ref. 101. Copyright 2016, AIP Publishing.

chemical carrier doping (Fig. 8a and b),^{99,100} representing an electron carrier-mediated exchange interaction. Although divalent Co has been supposed to substitute the Ti site, a recent study of X-ray fluorescence holography indicated a local suboxidic coordination of CoO_2Ti_4 (Fig. 8d and f) in ferromagnetic rutile $(\text{Ti},\text{Co})\text{O}_2$, whereas ordinary substitution of Co at the rutile Ti site was observed in paramagnetic $(\text{Ti},\text{Co})\text{O}_2$ with low Co concentration (Fig. 8c and e).¹⁰¹ In spite of the unclear relationship between the high temperature ferromagnetism and the suboxide structure, this result suggests that formation of hidden local structures in doped oxides is a new strategy to design novel functionalities.

3.3 Unusual valence state

Owing to the advanced thin film techniques introduced in section 2, unusual valence states can be stabilized in thin films. Since an unusual valence state could lead to unconventional electronic states, chemical control of such valences is a possible way to find novel functionalities.

Recently, epitaxial thin films of rock salt YO with unstable Y^{2+} ($4d^1$) were synthesized using the non-equilibrium condition of the PLD process.¹⁰² Here, Y metal was used as a target and the unusual valence state was attained under precise control of minute partial oxygen pressure during growth by using Ar/ O_2 mixed gas. In contrast with the band insulator Y_2O_3 with Y^{3+} , YO behaved as a narrow gap semiconductor and exhibited tuneable electrical conduction as a function of the amount of oxygen vacancy. The magnetoresistance showed weak antilocalization behaviour, which is attributed to strong spin-orbit coupling in the conducting 4d electrons.

ThCr_2Si_2 type $\text{R}_2\text{O}_2\text{Bi}$ (R = rare earth or Y) has another unusual valence compound with a Bi^{2-} square net, recently synthesized in a polycrystalline-powder form.¹⁰³ To obtain epitaxial thin films of $\text{Y}_2\text{O}_2\text{Bi}$, reductive solid phase epitaxy was adopted.¹⁰⁴ Y and Bi powders sandwiched between PLD-deposited Y_2O_3 amorphous films on CaF_2 substrates were subjected to two-step heating in an Ar + H_2 flow: the first low-temperature heating for alloying Bi and Y to reduce Bi by Y with a low redox potential, and the second high-temperature heating for solid phase epitaxy of the $\text{Y}_2\text{O}_2\text{Bi}$ phase. This method was significantly improved by one step *in situ* heating of multilayer precursor $[\text{Y}/\text{Bi}/\text{Y}_2\text{O}_3]_{25}$ with subnanometre layers (Fig. 9).¹⁰⁵ The obtained films possessed high crystallinity and a flat surface, which allowed observation of intrinsic magnetoresistance reflecting the 2D nature and strong spin-orbit interaction of the Bi^{2-} square net. Furthermore, this investigation resulted in the discovery of 2 K superconductivity in bulk $\text{Y}_2\text{O}_2\text{Bi}$ polycrystal with excess oxygen.¹⁰⁶

3.4 Anion substitution

Instead of cation substitution in complex oxides frequently used for chemical modification, anion substitution is prevailing as an alternative route to synthesize new functional compounds. Hydride (H^-), fluoride (F^-), and nitride (N^{3-}) ions

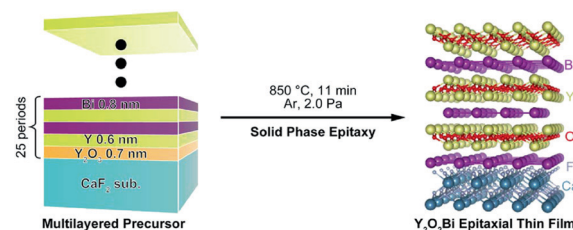


Fig. 9 Schematic illustration of the synthetic procedure of $\text{Y}_2\text{O}_2\text{Bi}$ epitaxial thin film via solid phase epitaxy. Reproduced with permission from ref. 105. Copyright 2015, American Chemical Society.

can substitute oxygen sites in oxides owing to their similar ionic radii, thus mixed-anion oxides such as oxyhydrides, oxyfluorides, and oxynitrides have been synthesized with a broad range of chemical compositions and crystal structures.¹⁰⁷ However, the fundamental properties of these mixed-anion oxides have been scarcely investigated because of the difficulty in high quality synthesis. Topotactic synthesis usually used for bulk specimens requires severe synthetic conditions such as high temperature and pressure for the reaction between stable oxide precursors and anion sources, resulting in an uncontrollable composition, structure, and homogeneity. In contrast, epitaxial thin film growth has several advantages such as a homogeneous milder post-deposition reaction,⁶⁹ direct synthetic route under finely tuned conditions,¹⁰⁸ and structural stabilization *via* epitaxial force.^{109,110}

Oxyhydride epitaxial films were prepared by reaction of oxide precursor films with hydration reagents such as CaH_2 . The hydride ion serves as an electron donor enabling heavy and tuneable electron doping. Yajima *et al.* and Bouilly *et al.* reported insulator-to-metal transition in $\text{ATiO}_{3-x}\text{H}_x$ (A = Ca, Sr and Ba) epitaxial thin films by hydridation,^{111,112} in which the electrical conductivity was systematically tuned in the range of $0 \leq x \leq 0.5$. The same group transformed an anti-ferromagnetic insulator EuTiO_3 epitaxial thin film into a ferromagnetic metal $\text{EuTiO}_{2.79}\text{H}_{0.21}$ film with a Curie temperature of 12 K,¹¹³ which is higher than those of $\text{EuTiO}_{3-\delta}$, (Eu, La) TiO_3 , and $\text{Eu}(\text{Ti},\text{Cr})\text{O}_3$, suggesting a smaller chemical disorder in $\text{EuTiO}_{2.79}\text{H}_{0.21}$. Katayama *et al.* obtained the first non-layered perovskite Sr-Co-O system, *c*-axis oriented SrCoO_xH_y ($x = 1.6 \pm 0.3$, $y = 1.2 \pm 0.2$) film, from brownmillerite $\text{SrCoO}_{2.5}$ film by topotactic reaction with CaH_2 .¹¹⁴ Here, SrCoO_xH_y was formed not on LSAT substrate but on STO substrate with a smaller lattice mismatch owing to the epitaxial stabilization. The shorter *b*- and *c*-axis length (0.370 and 0.3702 nm) than the *a*-axis length (0.416 nm) indicated the preferential formation of a 2D Co-H-Co network in the *bc* plane rather than random 3D distribution of hydrogen, probably causing the splitting of t_{2g} orbitals and bandgap widening from 0.35 eV of $\text{SrCoO}_{2.5}$ to 2.1 eV of SrCoO_xH_y .

Moon *et al.* reported the fluorination of brownmillerite $\text{SrFeO}_{3-\delta}$ ($\delta \sim 0.5$) into perovskite oxyfluoride $\text{SrFeO}_{3-\alpha}\text{F}_\alpha$.¹¹⁵ Poly(vinylidene fluoride) (PVDF) spin-cast on the film was

used as a fluorination reagent by annealing in an oxygen flow at 600 °C. $\text{SrFeO}_{3-\alpha}\text{F}_\gamma$ was semiconducting with a mixed valence state of Fe^{3+} and Fe^{4+} , reflecting the insulating $\text{SrFeO}_{3-\delta}$ with Fe^{3+} and metallic SrFeO_3 with Fe^{4+} , respectively. Katayama *et al.* reported $\text{SrFeO}_{3-x}\text{F}_x$ epitaxial thin films by reaction of $\text{SrFeO}_{3-\delta}$ thin film with spatially isolated PVDF in an Ar gas flow at a low temperature of 100–270 °C.⁶⁹ The fluorine content in the $\text{SrFeO}_{3-x}\text{F}_x$ films increased with increasing reaction temperature up to 270 °C, and decomposed into SrF_2 and Fe_3O_4 at higher temperature. The fluorination reaction was promoted more by a larger amount of oxygen vacancy in $\text{SrFeO}_{3-\delta}$, and the fluorine amount x was widely varied in the range of $0.8 \leq x \leq 1.5$.

Highly stable oxynitrides in comparison with oxyhydrides and oxyfluorides have been widely investigated as pigments, photocatalysts, and phosphors due to their bandgap harvesting visible and ultraviolet light.¹¹⁶ Since nitrogen ions are difficult to introduce into oxides with topotactic reactions partly due to the very low diffusion coefficient, the oxynitrides are usually powder specimens. Thus, the electrical properties have been scarcely investigated. In the case of epitaxial thin films, nitrogen can be *in situ* incorporated into oxides during film deposition by reactive rf magnetron sputtering,¹¹⁷ pulsed reactive crossed beam laser ablation,¹¹⁸ and other epitaxy techniques. Such thin films enable various characterization techniques.

The nitrogen plasma assisted pulsed laser deposition (NPA-PLD) method was adopted for perovskite CaTaO_2N epitaxial thin film.¹⁰⁷ In this method, nitrogen radicals were supplied from a plasma source during deposition of CaTaO_2N film on an STO substrate, where a $\text{Ca}_2\text{Ta}_2\text{O}_7$ sintered target was used. Compared to film specimens obtained by other methods,^{119,120} the CaTaO_2N film showed

smaller dielectric loss probably due to the high crystallinity and chemical homogeneity. A SrTaO_2N epitaxial thin film synthesized with the same method showed small classical ferroelectric regions surrounded by a relaxor-like matrix (Fig. 10a–d).¹⁰⁹ This result is in stark contrast to paraelectric or wholly relaxor-like bulk SrTaO_2N specimens,^{119,121} possibly caused by stabilization of a *trans*-type anion coordination in the compressively strained epitaxial thin film according to the first principles calculation (Fig. 10e and f). Such strain engineering on anion coordination can be a new approach to tailor novel functionalities in mixed-anion oxide epitaxial thin films. Electrically conductive oxynitrides are also available with NPA-PLD. Suzuki *et al.* synthesized metastable anatase TaON epitaxial thin film with the aid of epitaxial stabilization.¹²² TaON showed a rather high mobility of $\sim 17 \text{ cm}^2 \text{ V}^{-1} \text{ s}^{-1}$ at room temperature with an electron density of $3.7 \times 10^{19} \text{ cm}^{-3}$ supplied from oxygen vacancy. Electrical properties such as electrical conductivity and magnetism were controlled by the nitrogen content in films like hydride in oxyhydrides. Takahashi *et al.* synthesized AX-type CoO_xN_y epitaxial thin film, in which the anion ratio $y/(x+y)$ was systematically controlled in the range from 0 to 0.63.¹²³ CoO_xN_y showed a structural phase transition from rock salt ($y/(x+y) < 0.5$) to zinc blend ($y/(x+y) > 0.5$) structure. For the former, insulator-to-metal transition was induced by increasing nitrogen up to $y/(x+y) > 0.34$, concomitant with a drastic increase in saturation magnetization near the phase boundary. Recently, a topotactic synthetic route for oxynitrides was developed by Yajima *et al.*¹²⁴ $\text{BaTiO}_{3-x}\text{H}_x$ precursor was transformed to $\text{BaTiO}_{3-x}\text{N}_{2x/3}$ *via* nitridation with NH_3 at an unusually low temperature of 375–550 °C, by utilizing the lability of hydride ions in oxyhydrides. The $\text{BaTiO}_{0.2}\text{N}_{0.4}$ epitaxial thin film maintained the ferroelectric nature of BaTiO_3 .

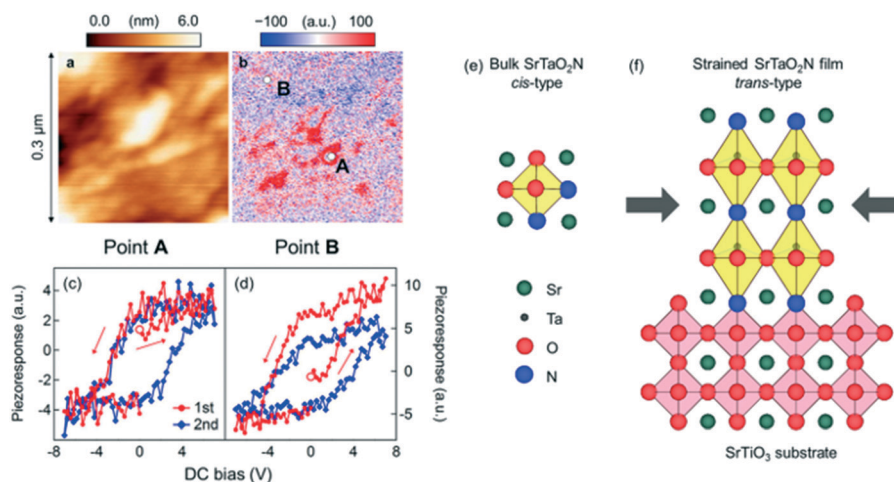


Fig. 10 (a) Topographic and (b) piezoresponse images of SrTaO_2N epitaxial thin film. (c and d) Local piezoresponse examined by switching spectroscopy at positions A and B in (b). (e and f) Schematics of (e) unstrained bulk SrTaO_2N with a *cis*-type anion arrangement and (f) tetragonally strained SrTaO_2N thin film with a *trans*-type anion arrangement epitaxially stabilized on SrTiO_3 substrate. Reproduced with permission from ref. 109. Copyright 2014, Macmillan Publishers Limited.

3.5 Epitaxial strain

Since the demonstration of enhanced Curie temperature in compressively strained BaTiO₃ epitaxial thin films,¹²⁵ the effects of epitaxial strain caused by lattice mismatch between film and substrate have been extensively investigated for various (quantum) ferroelectric compounds such as STO,¹²⁶ Pb(Zr,Ti)O₃,¹²⁷ and BiFeO₃,¹²⁸ recently reviewed by Damodaran *et al.*¹²⁹ Also, multiferroicity has been artificially generated by inducing ferroelectricity in magnetic compounds. Takahashi *et al.* reported single phase multiferroicity in ferromagnetic double perovskite La₂NiMnO₆ epitaxial thin film by appending ferroelectricity *via* lattice stretching along [111]_{cubic} on STO substrate.¹³⁰ It is noted that this ferroelectricity is driven by displacement of the A-site without lone pair electrons, as scarcely seen in perovskite oxides. Yun *et al.* reported high quality epitaxial thin films of metastable layered multiferroic Bi₆FeCoTi₃O₁₈ on a conducting LaNiO₃ buffer layer.¹³¹ LaNiO₃ significantly stabilized the film crystallization by preventing the divergence of electrical potential due to spontaneous polarization of the film through charge screening. The film showed phase switching in piezoresponse at room temperature, probably induced by the compressive strain from the substrate.

In addition to ferroelectricity, magnetism can also be controlled by strain because the bond angle between transition metal ions varies their exchange coupling, as demonstrated in (La,Sr)MnO₃ thin film on perovskite substrates decades ago.¹³² Yang *et al.* reported an anomalous phase diagram of La_{1-x}Sr_xCoO₃ under epitaxial strain.¹³³ Under tensile strain, ferromagnetism was induced in LaCoO₃ thin film due to a superexchange interaction between high spin-low spin-high spin Co³⁺ ions. On the other hand, ferromagnetism was strongly suppressed in La_{1-x}Sr_xCoO₃ ($x \sim 0.2$) thin film due to reduced double exchange coupling between Co³⁺ and Co⁴⁺ ions: the hole doping effect and local lattice strain caused by the introduction of Sr in addition to tensile strain assisted transition from high spin state Co³⁺ into low spin state Co⁴⁺ ions. Li *et al.* controlled interfacial magnetism between G-type antiferromagnetic SrMnO₃ (001) and

ferromagnetic (La,Sr)MnO₃ (001) epitaxial thin films *via* octahedral tilting tuned by strain as a function of SrMnO₃ thickness and type of substrate.¹³⁴ Here, the Dzyaloshinskii-Moriya (DM) interaction of the bilayer is expressed as $\bar{D}(\bar{S}_{\text{FM}} \times \bar{S}_{\text{AFM}})$, where \bar{D} denotes the DM vector and \bar{S}_{FM} and \bar{S}_{AFM} are spin vectors of FM and AFM layers, respectively. The DM interaction is finite only in case of out-of-phase tilting along the [100] direction in the antiferromagnetic layer under a magnetic field along the [010] direction (Fig. 11a). As expected by first principles calculation that the out-of-phase tilting along the [100] direction is stabilized under tensile strain, the most tensilely (compressively) strained film with the smallest SrMnO₃ thickness deposited on STO (LAO) showed the highest (lowest) exchange biases, and the strain effect relaxed gradually with increasing SrMnO₃ thickness (Fig. 11b and c).

Intriguingly, an epitaxial strain effect on the physical properties was manifested not only at the film-substrate interface but also at the surface. Marin *et al.* reported significantly suppressed saturation magnetization and an enhanced coercive field in compressively or tensilely strained ferromagnetic (La,Ca)MnO₃ epitaxial films.¹³⁵ Electron holography revealed the presence of an about 20 nm thick antiferromagnetic layer around the surface region. As a consequence of the coupling effect between e_g orbital ordering and Jahn-Teller distortions induced by strain, in addition to the relaxation of long-range interaction at the surface, the antiferromagnetic ordering emerged only at the surface, yielding the exchange bias.

Hirai *et al.* suggested that oxygen deficient materials are suitable for strain engineering of physical properties.¹³⁶ Oxygen deficient perovskite SrFeO_{2.8} films with tensile strain showed metal-to-insulator transition accompanied by charge disproportionation of Fe^{3.66+} into Fe³⁺ and Fe⁴⁺ at 620 K far above that of the bulk specimen, 70 K. The amount of oxygen deficiency itself was varied by epitaxial strain. Petrie *et al.* reported the formation of intermediate oxidation states SrCoO_{3-δ} between perovskite SrCoO₃ and brownmillerite SrCoO_{2.5} under tensile strain.¹³⁷ With increasing tensile

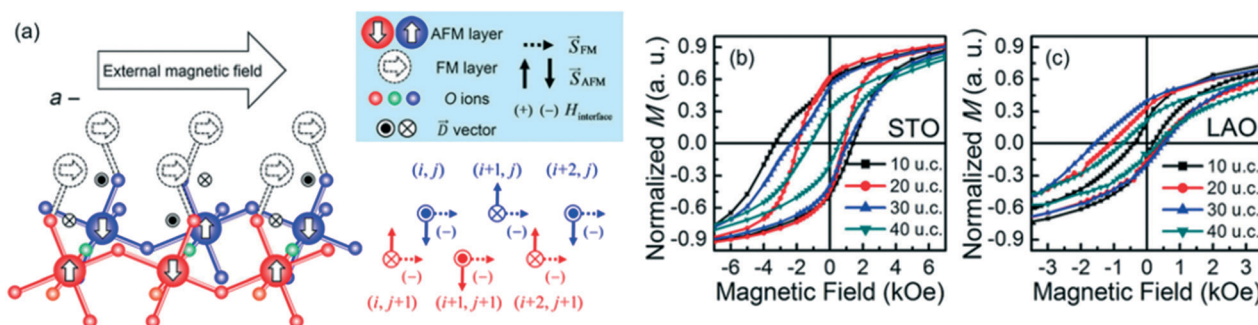


Fig. 11 (a) Sketch of the G-type antiferromagnetic/ferromagnetic interface given for antiphase tilting about the [100] (a axis) with the sign of the Dzyaloshinskii-Moriya interaction term shown in the right simplified diagram for the whole interface. (b and c) Magnetization curves of (La,Sr)MnO₃ (20 u.c.)/SrMnO₃ (t) on STO (b) and LAO (c) for different SrMnO₃ thicknesses ($t = 10, 20, 30$, and 40 u.c.). Reproduced with permission from ref. 134. Copyright 2015, Macmillan Publishers Limited.

strain from 1.0% to 4.2%, δ linearly increased from 0.1 to 0.25, resulting in ferromagnetic metal to antiferromagnetic insulator transition. According to calculation, tensile strain destabilized the ground state due to the reduced intercalation formation enthalpy of oxygen, giving a route to modify oxygen conduction in oxides. Farokhipoor *et al.* reported epitaxial strain control of cation deficient domain wall density in a multiferroic system.¹³⁸ Tensilely strained TbMnO₃ film on STO substrate with a lattice mismatch of 5% showed dense formation of the domain walls which occupy as high as 25% of total film volume to release the large strain (Fig. 12a). At the domain wall, Tb was replaced by Mn (Fig. 12b and c) to enhance net magnetization (Fig. 12d and e). Such artificial control of local lattice structure can be used to form novel crystal structures and functionalities.

3.6 Defect formation

As mentioned in section 2, it is often difficult to transfer stoichiometric composition from source to film. Even in the case of PLD, off-stoichiometric thin films are often deposited. As reported by Ohnishi *et al.*, laser fluence is one of the most significant factors that govern the film composition,¹³⁹ suggesting that the kinetic energy of the chemical species during deposition influences the chemical composition in thin films by defect formation. Such defects in epitaxial films and heteroepitaxial structures usually cause undesired effects on the physical properties, but recently have been exploited to develop novel functionalities. Lee *et al.* controlled the amount and site of vacancies in STO thin films systematically by growth condition.¹⁴⁰ The *c*-axis lattice constant, propor-

tional to the amount of Sr vacancy, was increased by laser energy, while an insulator-to-metal transition accompanied by reduced transmittance was induced by introducing an oxygen vacancy *via* oxygen flow rate without significant change in the lattice parameter. Sarantopoulos *et al.* precisely controlled the amount of Sr and O vacancies in STO epitaxial thin films by changing the partial oxygen pressure during PLD growth.¹⁴¹ Uniform tetragonal distortion along 50 nm thick film due to Sr vacancy, in spite of the presence of film/substrate interfacial defects, resulted in splitting of t_{2g} states coupled with the spin-orbit interaction. The lowered degeneracy was manifested as the emergence of an anomalous Hall effect and anisotropic magnetoresistance, similar to LAO/STO interfaces and quantum wells, possibly caused by long range magnetic ordering.

Defect induced strain is an efficient way to modulate ferroelectricity like lattice mismatch induced strain. Damodaran *et al.* reported significant *c*-axis expansion of up to 4.1% in PLD-deposited stoichiometric BaTiO₃ films with increasing laser fluence (Fig. 13a).¹⁴² This expansion was attributed to dipole formation from charged point defects along the out-of-plane direction in addition to the compressive epitaxial strain from GdScO₃ substrates. These defects enhanced the Curie temperature up to 800 °C without impairing insulating properties (Fig. 13b and c).

Recently, ferroelectric-like behaviours were observed using piezoelectric force microscopy in heterostructures composed of non-ferroelectric oxides such as STO, TiO₂,¹⁴³ and LAO.¹⁴⁴ Sharma *et al.* investigated LAO epitaxial thin films deposited on the lattice-matched conducting Sr_{0.2}Ca_{0.8}RuO₃ bottom layer on LSAT substrate.¹⁴⁵ By excluding extrinsic effects such

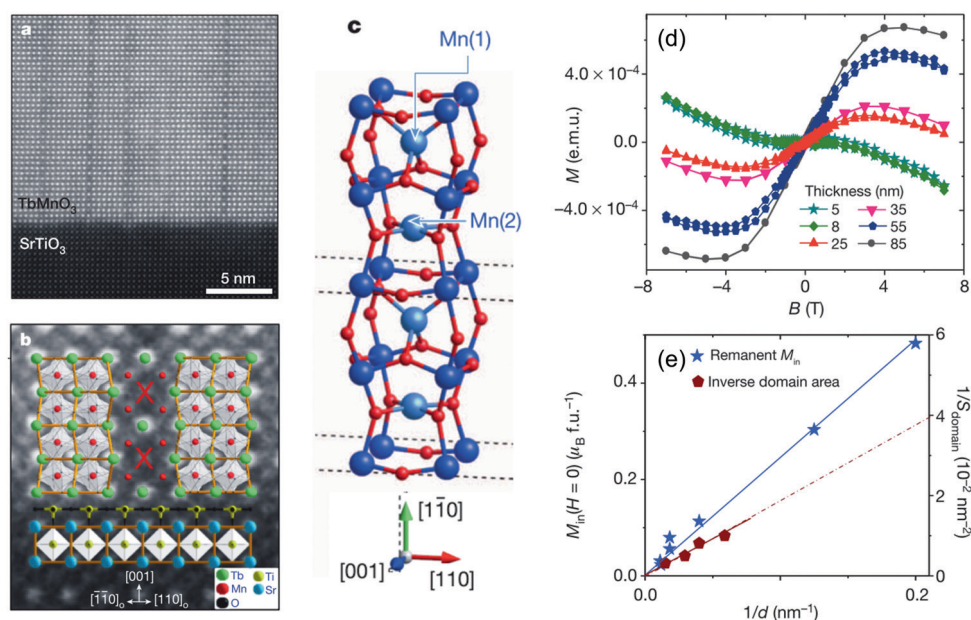


Fig. 12 (a) HAADF-STEM image of TbMnO₃-SrTiO₃ interface. (b) Domain wall in TbMnO₃ close to the interface with SrTiO₃, superposed on the proposed atomic model. (c) Proposed columnar structure of substitutional Mn cations (light blue) at domain wall. (d) In-plane magnetization curves at 10 K for TbMnO₃ films with various thicknesses. (e) Remanent magnetization *versus* inverse of film thickness. The inverse domain area (or density of domain walls) is also plotted. Reproduced with permission from ref. 138. Copyright 2014, Macmillan Publishers Limited.

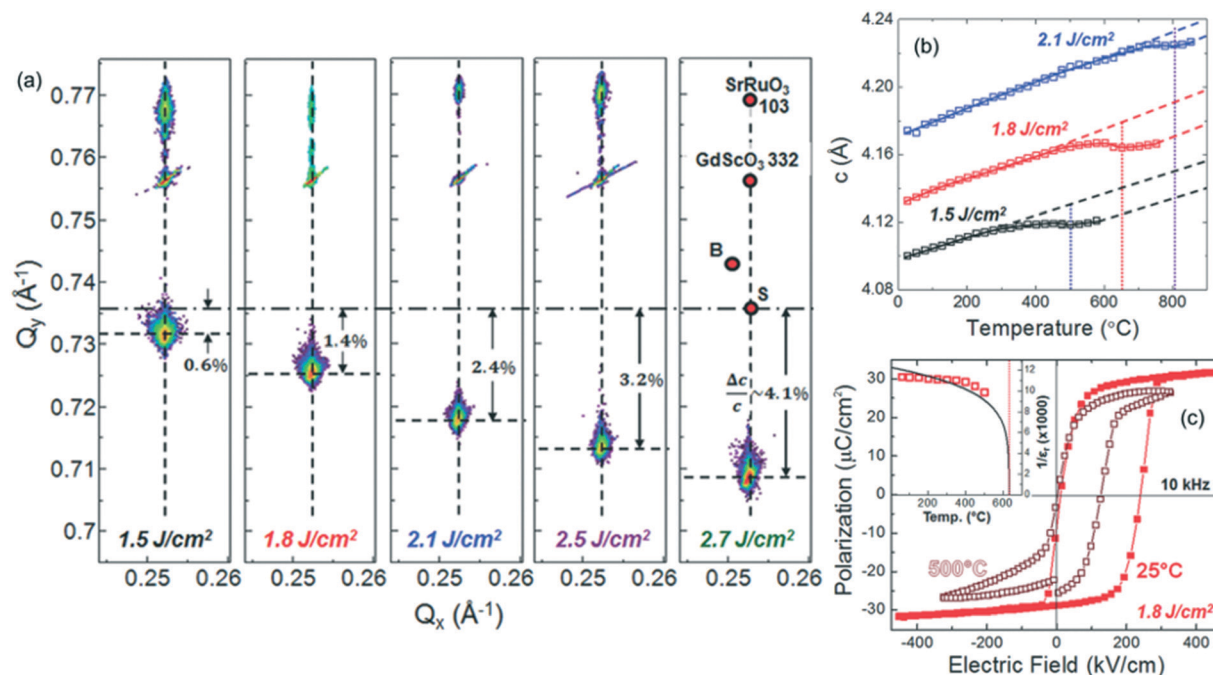


Fig. 13 (a) Reciprocal space maps around the 103- and 332-diffractions of BaTiO₃ films and GdScO₃ substrate as a function of laser fluence of 1.5, 1.8, 2.1, 2.5, and 2.7 J cm⁻². (b) Temperature dependence of out-of-plane c -axis lattice parameters with different laser fluences for BaTiO₃/SrRuO₃/GdScO₃ (110) heterostructures. (c) Ferroelectric hysteresis loops for the heterostructure grown at 1.8 J cm⁻², revealing the presence of strong polarization even at 500 °C. The inset shows the evolution of the polarization from 25 to 500 °C. Reproduced with permission from ref. 142. Copyright 2014, John Wiley & Sons, Inc.

as surface charge effects and current induced electromechanical responses, the ferroelectric-like behaviour was attributed to bistable distributions of ions and oxygen-vacancies in the films. The stable distributions were switched not only by an external electric field but also by mechanical force with an atomic force microscope tip. The latter corresponds to a flexoelectric effect generating an internal electric field proportional to the applied stress. Such a ferroelectric-like response caused by ion/vacancy migration was suggested for potential switching applications with mechanical-write and electrical-read.

3.7 Substructure propagation

Chemical bonding across the film/substrate heterointerface is associated with not only lattice matching but also substructure propagation as seen in the octahedral rotation in perovskite heterostructures. The latter is an interesting effect because the chemical bonding angle significantly affects physical properties such as optical band gap, magnetism, and polarity.

The propagation effects of octahedral rotation in perovskite heterostructures were suggested earlier than direct or indirect observation.^{146–149} Recently, Aso *et al.* directly observed in-phase octahedral rotation around the [001]_{ortho} direction near the interface of perovskite SrRuO₃ film on GaScO₃ substrate, in which both crystals have a *Pbmn* orthorhombic structure.¹⁵⁰ The RuO₆ octahedron in the thin film was forced to rotate in order to match the rotation angle of

the ScO₆ octahedron in the substrate, whereas the topmost apical oxygen in the ScO₆ octahedron was dragged from its original site because of their largely different octahedral tilt angle θ ($\theta = 168^\circ$ and 156° for SrRuO₃ and GdScO₃, respectively). The substructure propagation was relieved within only 4 unit cells while the in-plane lattice parameter of the film was perfectly locked. The rotation angle in the film was controlled by inserting a buffer layer. In the case of the BaTiO₃ buffer layer, SrRuO₃ transformed into the tetragonal phase due to the large ionic radius of Ba, resulting in strong suppression of octahedral rotation.¹⁵¹ On the other hand, the tilt angle was controllably reduced by inserting a Ca_{0.5}Sr_{0.5}TiO₃ layer with different thicknesses from 1 u.c. to 4 u.c.: $\theta = 180^\circ$ for 4 u.c. as in the case of the BaTiO₃ buffer layer (Fig. 14a–h).¹⁵² Interestingly, the rotation angle was constant along the whole thickness of the SrRuO₃ layer probably due to the bistability of the orthorhombic phase ($\theta = 168^\circ$) and tetragonal phase ($\theta = 180^\circ$). The influence of the octahedral rotation angle on the electronic structure was manifested as magnetic anisotropy of ferromagnetic SrRuO₃ thin films. The easy magnetization axis was rotated by about 45° at $\theta \approx 175^\circ$ (Fig. 14i). The details were recently reviewed elsewhere.¹⁵³

The substructure propagation is observed in various epitaxial thin films. Liao *et al.* observed a large octahedral rotation propagated from NdGaO₃ substrates to adjacent 4 u.c. layers in (La,Sr)MnO₃ epitaxial thin films.¹⁵⁴ The magnetic easy axis was rotated from the original b -axis in bulk to the a -axis as was not observed in the films on the STO buffer layer,

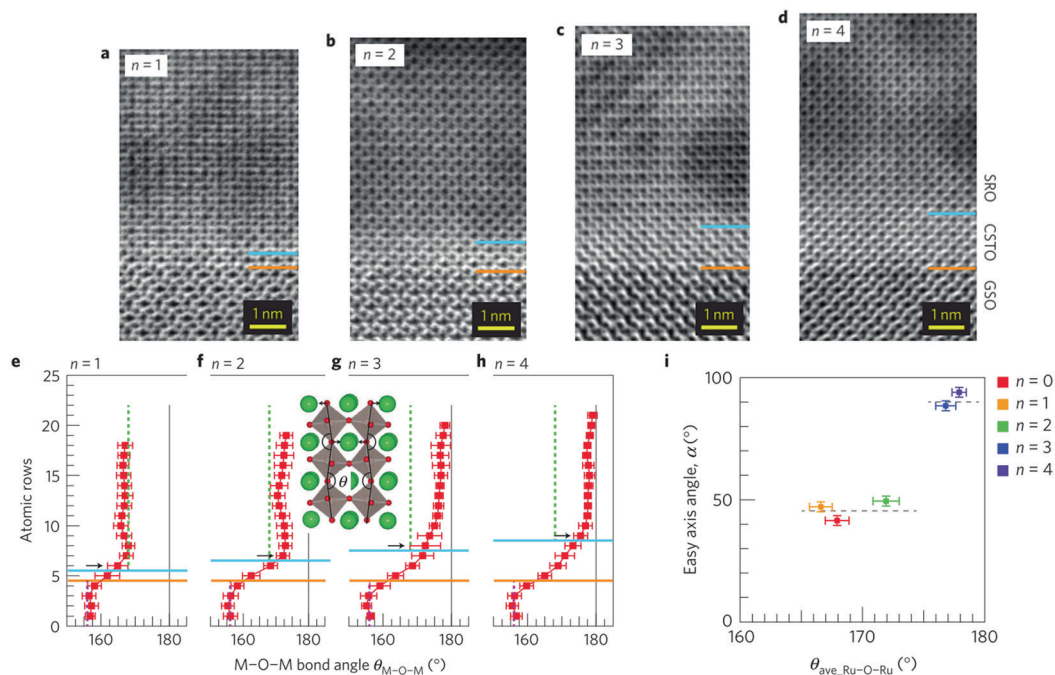


Fig. 14 (a–d) ABF-STEM images for the (a) $n = 1$, (b) $n = 2$, (c) $n = 3$, and (d) $n = 4$ $\text{SrRuO}_3/[\text{Ca}_{0.5}\text{Sr}_{0.5}\text{TiO}_3]_n/\text{GdScO}_3$ heterostructures. Blue and orange lines denote $\text{SrRuO}_3/\text{Ca}_{0.5}\text{Sr}_{0.5}\text{TiO}_3$ and $\text{Ca}_{0.5}\text{Sr}_{0.5}\text{TiO}_3/\text{GdScO}_3$ interfaces, respectively. (e–h) M–O–M bond angle $\theta_{\text{M-O-M}}$ (M = Sc, Ti, and Ru) as a function of atomic position in (e) $n = 1$, (f) $n = 2$, (g) $n = 3$ and (h) $n = 4$. (i) Magnetization easy axis angle α as a function of the Ru–O–Ru bond angle $\theta_{\text{ave_Ru-O-Ru}}$ in the SrRuO_3 layer. Reproduced with permission from ref. 152. Copyright 2014, Macmillan Publishers Limited.

indicating that the large octahedral rotation induces the magnetic anisotropy rotation. Qiao *et al.* investigated the influence of symmetry mismatch on LaCoO_3 epitaxial thin

films.¹⁵⁵ Magnetism significantly depended on the LaCoO_3 film thickness on STO substrates: moderately correlated diamagnetic behaviour for 5 u.c. thick film and strongly

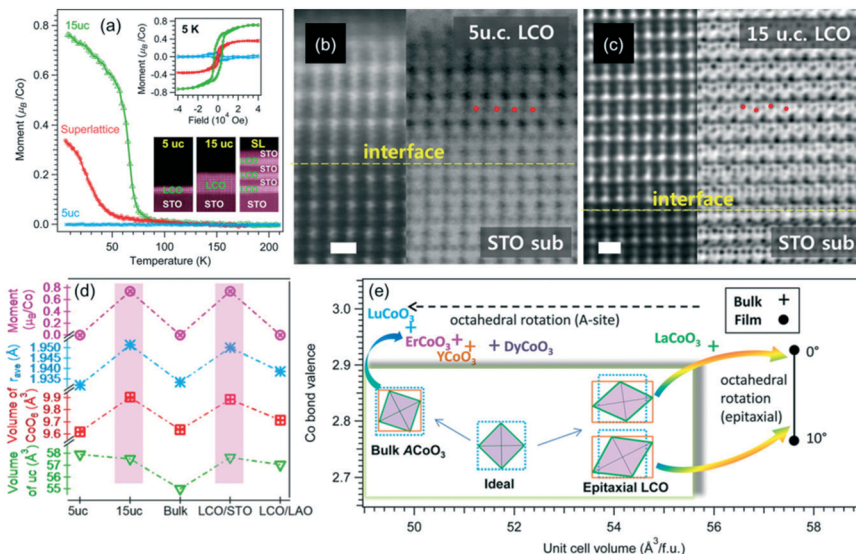


Fig. 15 (a) Temperature dependence of magnetization for $\text{LaCoO}_3/\text{STO}$ films and superlattice at 1000 Oe under field-cooling. The top inset shows magnetic hysteresis curves at 5 K. The bottom inset shows low-magnification cross sectional HAADF images. (b) and (c) HAADF (left)/ABF (right) images of (b) 5 u.c. and (c) 15 u.c. LaCoO_3 films in the $[110]$ projection. Red dots represent the oxygen columns in LaCoO_3 film. (d) Magnetization and structural parameters for LaCoO_3 films as well as referential data of bulk LaCoO_3 and 20 nm epitaxial LaCoO_3 on STO and LAO substrates. (e) Bond valence of Co as a function of cell volume for different perovskite Co^{3+} bulk compounds and epitaxial LaCoO_3 , with and without octahedral rotations, based on the experimental structures. The inset shows schematic changes in unit cell volume and CoO_6 octahedral distortion for ACoO_3 bulk perovskites and epitaxial LaCoO_3 films. Reproduced with permission from ref. 155. Copyright 2015, American Chemical Society.

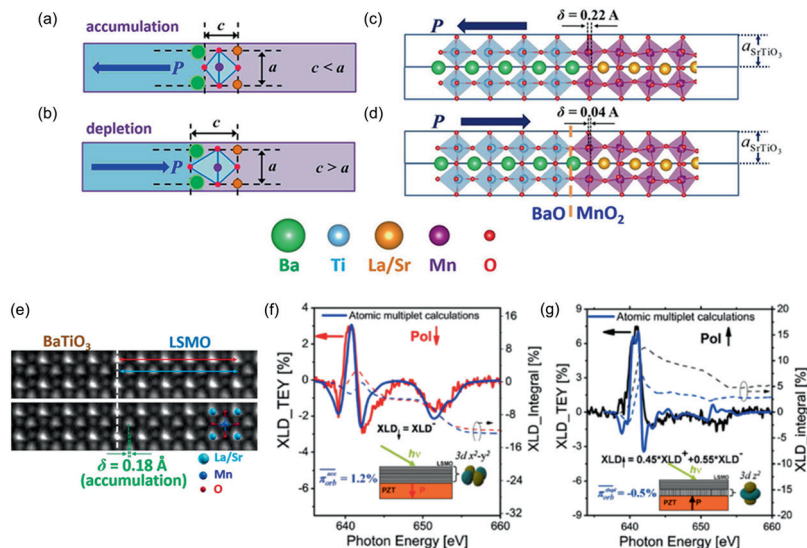


Fig. 16 (a and b) Schematic BaO/MnO₂ interfaces of BaTiO₃/(La,Sr)MnO₃ heterostructure in (a) accumulation and (b) depletion states. The purple and light blue parts represent (La,Sr)MnO₃ and BaTiO₃, respectively. (c and d) Relaxed atomic structure of the interfaces in (c) accumulation and (d) depletion states from first-principles calculations. (e) ABF image of the interface in accumulation state. Reproduced with permission from ref. 156. Copyright© 2014 American Chemical Society. (f and g) Experimental and theoretical X-ray linear dichroism spectra for a (La,Sr)MnO₃ epitaxial film on Pb(Zr,Ti)O₃ in (f) accumulation and (g) depletion states. Reproduced with permission from ref. 157. Copyright 2015, American Physical Society.

correlated ferromagnetic behaviour for 15 u.c. thick film (Fig. 15a and d). The strong correlation for the latter can be rationalized by the decrease of crystal field splitting caused by expansion of CoO₆ octahedra under tensile strain. The accompanying octahedral tilt decreases Co–O bond covalency which favours magnetic order (Fig. 15c and e). On the other hand the moderate correlation and diamagnetism in the thinner film was caused by suppressed octahedral tilting due to mismatch in the octahedral rotation angle (Fig. 15b and e). The authors proposed that heteroepitaxial strain introduces volume change in the octahedron more efficiently than chemical substitution does.

Out-of-plane atomic displacement of substructure in a polar substrate also propagates into the film. Chen *et al.* investigated the structural change in ferromagnetic (La,Sr)MnO₃ epitaxial films on 20 u.c. thick ferroelectric BaTiO₃ bottom layers.¹⁵⁶ In the case of the spontaneous polarization in BaTiO₃ backward to the interface, hole accumulation and structural asymmetry at the interface caused a shift of Mn ions in phase with that of Ti ions in BaTiO₃ accompanied by a small decrease of c/a , resulting in broken degeneracy of Mn e_g orbitals to stabilize the $d_{x^2-y^2}$ orbital (Fig. 16a, c and e). In the case of the opposite spontaneous polarization, hole depletion caused tetragonal distortion ($c/a > 1$) of the (La,Sr)MnO₃ unit cell, resulting in broken degeneracy of Mn e_g orbitals to destabilize the $d_{x^2-y^2}$ on the contrary (Fig. 16b and d). Accordingly, the d electron population in the transition metal oxide film was controlled by switching spontaneous polarization in the adjacent ferroelectric layer. Later, Preziosi *et al.* observed the change in electron population of Mn e_g orbitals by polarization switching in (La,Sr)MnO₃ epitaxial thin film

on Pb(Zr,Ti)O₃ layer by means of X-ray linear dichroism (Fig. 16f and g).¹⁵⁷

4 Outlook

In this review, we presented recent advances in growth techniques of functional oxide epitaxial thin films and their crystal engineering for novel functionalities. Atomic-scale control of films is possible from aspects of both chemical composition and crystal structure. Accordingly, research fields utilizing oxide epitaxy technology are rapidly spreading: oxide ionics,^{158–161} interface phenomena¹⁶ such as formation of 2DEG^{162–166} and topological states,¹⁶⁷ low dimensional electronics,^{168–170} quantum effects,¹⁷¹ and 4d/5d oxide electronics.^{172,173} In order to develop these fields further, comprehensive understanding of not only the film growth processes including metastable structure formation and ionic migration but also the atomic-scale electronic states at the interface and the ultrathin layer and of interplay between electron, spin, and orbital are indispensable. To this end, cutting edge thin film growth methods and atomic-scale analytical tools are important. Crystal engineering of functional oxides is important for not only basic science but also practical applications, contributing to the discovery of novel phenomena and invention of next generation applications. In addition, the development of oxide thin film epitaxy will merge modern silicon and III–V semiconductor technologies and oxide electronics. The crystal engineering of oxides even on non-oxide substrates is possible.^{174,175} Also, organic–inorganic hybrid devices are under investigation.^{176,177} The combination of oxides with different classes of materials would further expand these emerging research fields.

Acknowledgements

This work was in part supported by Core Research for Evolutionary Science and Technology of Japan Science and Technology Agency and JSPS KAKENHI (26600091, 26105002).

References

- J. Heber, *Nature*, 2009, **459**, 28–30.
- Functional Metal Oxides: New Science and Novel Applications*, ed. S. B. Ogale, T. V. Venkatesan and M. Blamire, Wiley-VCH, 2013.
- M. Lorenz, M. S. Ramachandra Rao, T. Venkatesan, E. Fortunato, P. Barquinha, R. Branquinho, D. Salgueiro, R. Martins, E. Carlos, A. Liu, F. K. Shan, M. Grundmann, H. Boschker, J. Mukherjee, M. Priyadarshini, N. Das Gupta, D. J. Rogers, F. H. Teherani, E. V. Sandana, P. Bove, K. Rietwyk, A. Zaban, A. Veziridis, A. Weidenkaff, M. Muralidhar, M. Murakami, S. Abel, J. Fompeyrine, J. Zuniga-Perez, R. Ramesh, N. A. Spaldin, S. Ostanin, V. Borisov, I. Mertig, V. Lazenka, G. Srinivasan, W. Prellier, M. Uchida, M. Kawasaki, R. Pentcheva, P. Gegenwart, F. Miletto Granozio, J. Fontcuberta and N. Pryds, *J. Phys. D: Appl. Phys.*, 2016, **49**, 433001.
- H. Hosono, *Thin Solid Films*, 2007, **515**, 6000–6014.
- L. Martin, Y. Chu and R. Ramesh, *Mater. Sci. Eng., R*, 2010, **68**, 89–133.
- K. F. Wang, J.-M. Liu and Z. F. Ren, *Adv. Phys.*, 2009, **58**, 321–448.
- K. D. Kreuer, *Annu. Rev. Mater. Res.*, 2003, **33**, 333–359.
- M. Imada, A. Fujimori and Y. Tokura, *Rev. Mod. Phys.*, 1998, **70**, 1039–1263.
- A. P. Ramirez, *Science*, 2007, **315**, 1377–1378.
- J. G. Bednorz and K. A. Muller, *Z. Phys. B: Condens. Matter*, 1986, **64**, 189–193.
- H. Koinuma, *Solid State Ionics*, 1998, **108**, 1–7.
- Crystal Engineering of High-Tc-related Oxide Films (special issue)*, ed. H. Koinuma, MRS Bull., 1994, vol. 19.
- H. Koinuma, *Thin Solid Films*, 2005, **486**, 2–10.
- M. Kawasaki, *Bull. Chem. Soc. Jpn.*, 2013, **86**, 1341–1358.
- F. J. Wong and S. Ramanathan, *J. Vac. Sci. Technol., A*, 2014, **32**, 40801.
- H. Y. Hwang, Y. Iwasa, M. Kawasaki, B. Keimer, N. Nagaosa and Y. Tokura, *Nat. Mater.*, 2012, **11**, 103–113.
- M. Ziese and I. Vrejoiu, *Phys. Status Solidi RRL*, 2013, **7**, 243–257.
- H.-J. Liu, W.-I. Liang, Y.-H. Chu, H. Zheng and R. Ramesh, *MRS Commun.*, 2014, **4**, 31–44.
- J. L. Macmanus-Driscoll, *Adv. Funct. Mater.*, 2010, **20**, 2035–2045.
- J. J. Cuomo, D. L. Pappas, J. Bruley, J. P. Doyle and K. L. Saenger, *J. Appl. Phys.*, 1991, **70**, 1706–1711.
- M. N. R. Ashfold, F. Claeysens, G. M. Fuge and S. J. Henley, *Chem. Soc. Rev.*, 2004, **33**, 23–31.
- H. M. Christen and G. Eres, *J. Phys.: Condens. Matter*, 2008, **20**, 264005.
- R. K. Singh and J. Narayan, *Phys. Rev. B: Condens. Matter Mater. Phys.*, 1990, **41**, 8843–8859.
- T. Ohnishi, H. Koinuma and M. Lippmaa, *Appl. Surf. Sci.*, 2006, **252**, 2466–2471.
- S. Ohashi, M. Lippmaa, N. Nakagawa, H. Nagasawa, H. Koinuma and M. Kawasaki, *Rev. Sci. Instrum.*, 1999, **70**, 178–183.
- T. Koida, D. Komiyama, H. Koinuma, M. Ohtani, M. Lippmaa and M. Kawasaki, *Appl. Phys. Lett.*, 2002, **80**, 565–567.
- H. Koinuma and I. Takeuchi, *Nat. Mater.*, 2004, **3**, 429–438.
- M. Lippmaa, N. Nakagawa, M. Kawasaki, S. Ohashi and H. Koinuma, *Appl. Phys. Lett.*, 2000, **76**, 2439–2441.
- T. M. Shaw, A. Gupta, M. Y. Chern, P. E. Batson, R. B. Laibowitz and B. A. Scott, *J. Mater. Res.*, 1994, **9**, 2566–2573.
- T. Ohnishi, D. Komiyama, T. Koida, S. Ohashi, C. Stauter, H. Koinuma, A. Ohtomo, M. Lippmaa, N. Nakagawa, M. Kawasaki, T. Kikuchi and K. Omote, *Appl. Phys. Lett.*, 2001, **79**, 536–538.
- Handbook of Thin Film Deposition (Third Edition)*, ed. K. Seshan, Elsevier, 2012.
- V. S. Smentkowski, *Prog. Surf. Sci.*, 2000, **64**, 1–58.
- P. Willmott, *Prog. Surf. Sci.*, 2004, **76**, 163–217.
- P. J. Martin, *J. Mater. Sci.*, 1986, **21**, 1–25.
- E. Bousquet, M. Dawber, N. Stucki, C. Lichtensteiger, P. Hermet, S. Gariglio, J.-M. Triscone and P. Ghosez, *Nature*, 2008, **452**, 732–736.
- J. Garcia-Barriocanal, A. Rivera-Calzada, M. Varela, Z. Sefrioui, E. Iborra, C. Leon, S. J. Pennycook and J. Santamaria, *Science*, 2008, **321**, 676–680.
- F. Baiutti, G. Christiani and G. Logvenov, *Beilstein J. Nanotechnol.*, 2014, **5**, 596–602.
- A. A. Baker, W. Braun, G. Gassler, S. Rembold, A. Fischer and T. Hesjedal, *Rev. Sci. Instrum.*, 2015, **86**, 043901.
- K. Horiba, H. Ohguchi, H. Kumigashira, M. Oshima, K. Ono, N. Nakagawa, M. Lippmaa, M. Kawasaki and H. Koinuma, *Rev. Sci. Instrum.*, 2003, **74**, 3406–3412.
- C. D. Theis, J. Yeh, D. G. Schlom, M. E. Hawley and G. W. Brown, *Thin Solid Films*, 1998, **325**, 107–114.
- B. Jalan, P. Moetakef and S. Stemmer, *Appl. Phys. Lett.*, 2009, **95**, 32906.
- A. Tsukazaki, S. Akasaka, K. Nakahara, Y. Ohno, H. Ohno, D. Maryenko, A. Ohtomo and M. Kawasaki, *Nat. Mater.*, 2010, **9**, 889–893.
- B. Jalan, R. Engel-Herbert, N. J. Wright and S. Stemmer, *J. Vac. Sci. Technol., A*, 2009, **27**, 461–464.
- J. Son, P. Moetakef, B. Jalan, O. Bierwagen, N. J. Wright, R. Engel-Herbert and S. Stemmer, *Nat. Mater.*, 2010, **9**, 482–484.
- Y. Matsubara, K. S. Takahashi, M. S. Bahramy, Y. Kozuka, D. Maryenko, J. Falson, A. Tsukazaki, Y. Tokura and M. Kawasaki, *Nat. Commun.*, 2016, **7**, 11631.
- S. Vallejos, F. Di Maggio, T. Shujah and C. Blackman, *Chemosensors*, 2016, **4**, 4.
- T. Goto, *J. Wuhan Univ. Technol., Mater. Sci. Ed.*, 2016, **31**, 1–5.

- 48 K. Haga, M. Kamidaira, Y. Kashiwaba, T. Sekiguchi and H. Watanabe, *J. Cryst. Growth*, 2000, **214**–215, 77–80.
- 49 Y. Kuzminykh, A. Dabirian, M. Reinke and P. Hoffmann, *Surf. Coat. Technol.*, 2013, **230**, 13–21.
- 50 K. Sawada, M. Ishida, T. Nakamura and N. Ohtake, *Appl. Phys. Lett.*, 1988, **52**, 1672–1674.
- 51 K. Endo, Y. Mariyasu, S. Misawa and S. Yoshida, *Phys. C*, 1991, **185**–189, 1995–1996.
- 52 E. Mächler, F. Arrouy, E. Fritsch, J. G. Bednorz, H. Berke, J. R. Huber and J.-P. Locquet, *Appl. Phys. Lett.*, 1997, **71**, 710–712.
- 53 J. Lu, J. W. Elam and P. C. Stair, *Acc. Chem. Res.*, 2013, **46**, 1806–1815.
- 54 J. Lu, J. W. Elam and P. C. Stair, *Surf. Sci. Rep.*, 2016, **71**, 410–472.
- 55 M. D. McDaniel, T. Q. Ngo, S. Hu, A. Posadas, A. A. Demkov and J. G. Ekerdt, *Appl. Phys. Rev.*, 2015, **2**, 41301.
- 56 M. Coll, J. M. Montero Moreno, J. Gazquez, K. Nielsch, X. Obradors and T. Puig, *Adv. Funct. Mater.*, 2014, **24**, 5368–5374.
- 57 J. D. Emery, C. M. Schlepuz, P. Guo, R. P. H. Chang and A. B. F. Martinson, *Cryst. Growth Des.*, 2015, **16**, 640–645.
- 58 L. L. Hench and J. K. West, *Chem. Rev.*, 1990, **90**, 33–72.
- 59 Y. Zhao, P. Torres, X. Tang, P. Norby and J.-C. Grivel, *Inorg. Chem.*, 2015, **54**, 10232–10238.
- 60 S. T. Meyers, J. T. Anderson, D. Hong, C. M. Hung, J. F. Wager and D. A. Keszler, *Chem. Mater.*, 2007, **19**, 4023–4029.
- 61 B. Rivas-Murias, J. Manuel Vila-Funqueiriño and F. Rivadulla, *Sci. Rep.*, 2015, **5**, 11889.
- 62 S. Wang, A. Venimadhav, S. Guo, K. Chen, Q. Li, A. Soukiassian, D. G. Schlom, M. B. Katz, X. Q. Pan, W. Wong-Ng, M. D. Vaudin and X. X. Xi, *Appl. Phys. Lett.*, 2009, **94**, 22110.
- 63 T. Kawaharamura, *Jpn. J. Appl. Phys.*, 2014, **53**, 05FF08.
- 64 S. Fujita, K. Kaneko, T. Ikenoue, T. Kawaharamura and M. Furuta, *Phys. Status Solidi C*, 2014, **118**, 1225–1228.
- 65 K. Kaneko, K. Suzuki, Y. Ito and S. Fujita, *J. Cryst. Growth*, 2016, **436**, 150–154.
- 66 S. Yao, T. Sato, K. Kaneko, S. Murai, K. Fujita and K. Tanaka, *Jpn. J. Appl. Phys.*, 2015, **54**, 63001.
- 67 S. Murai, T. Sato, S. Yao, R. Kamakura, K. Fujita and K. Tanaka, *J. Lumin.*, 2016, **170**, 808–811.
- 68 L. S. D. Glasser, F. P. Glasser and H. F. W. Taylor, *Q. Rev., Chem. Soc.*, 1962, **16**, 343–360.
- 69 T. Katayama, A. Chikamatsu, Y. Hirose, R. Takagi, H. Kamisaka, T. Fukumura and T. Hasegawa, *J. Mater. Chem. C*, 2014, **2**, 5350–5356.
- 70 K. H. L. Zhang, P. V. Sushko, R. Colby, Y. Du, M. E. Bowden and S. A. Chambers, *Nat. Commun.*, 2014, **5**, 4669.
- 71 K. Yoshimatsu, M. Niwa, H. Mashiko, T. Oshima and A. Ohtomo, *Sci. Rep.*, 2015, **5**, 16325.
- 72 G. H. Haertling, *J. Am. Ceram. Soc.*, 1999, **82**, 797–818.
- 73 M. Dawber, K. M. Rabe and J. F. Scott, *Rev. Mod. Phys.*, 2005, **77**, 1083–1130.
- 74 Y. Tokura and N. Nagaosa, *Science*, 2000, **288**, 462–468.
- 75 O. Y. Gorbenko, S. V. Samoilenkov, I. E. Graboy and A. R. Kaul, *Chem. Mater.*, 2002, **14**, 4026–4043.
- 76 S. X. Zhang, D. C. Kundaliya, W. Yu, S. Dhar, S. Y. Young, L. G. Salamanca-Riba, S. B. Ogale, R. D. Vispute and T. Venkatesan, *J. Appl. Phys.*, 2007, **102**, 013701.
- 77 S. Chen, M. G. Mason, H. J. Gysling, G. R. Paz-Pujalt, T. N. Blanton, T. Castro, K. M. Chen, C. P. Fictorie, W. L. Gladfelter, A. Franciosi, P. I. Cohen and J. F. Evans, *J. Vac. Sci. Technol., A*, 1993, **11**, 2419–2429.
- 78 Y. Furubayashi, T. Hitosugi, Y. Yamamoto, Y. Hirose, G. Kinoda, K. Inaba, T. Shimada and T. Hasegawa, *Thin Solid Films*, 2006, **496**, 157–159.
- 79 T. Hitosugi, N. Yamada, S. Nakao, Y. Hirose and T. Hasegawa, *Phys. Status Solidi A*, 2010, **207**, 1529–1537.
- 80 D. Shinohara and S. Fujita, *Jpn. J. Appl. Phys.*, 2008, **47**, 7311–7313.
- 81 K. Kaneko, I. Takeya, S. Komori and S. Fujita, *J. Appl. Phys.*, 2013, **113**, 233901.
- 82 S. Lee, I. N. Ivanov, J. K. Keum and H. N. Lee, *Sci. Rep.*, 2016, **6**, 19621.
- 83 S. Lee, A. R. Damodaran, P. Gorai, N. Oh, J. A. Moyer, J. H. Kwon, N. Ferdous, A. Shah, Z. Chen, E. Breckenfeld, R. V. K. Mangalam, P. V. Braun, P. Schiffer, M. Shim, J. M. Zuo, E. Ertekin and L. W. Martin, *Adv. Mater.*, 2015, **27**, 861–868.
- 84 A. Janotti and C. G. Van de Walle, *Rep. Prog. Phys.*, 2009, **72**, 126501.
- 85 Y. Kozuka, A. Tsukazaki and M. Kawasaki, *Appl. Phys. Rev.*, 2014, **1**, 11303.
- 86 J. F. Sarver, F. L. Katnack and F. A. Hummel, *J. Electrochem. Soc.*, 1959, **106**, 960–963.
- 87 A. Ohtomo, M. Kawasaki, T. Koida, K. Masubuchi, H. Koinuma, Y. Sakurai, Y. Yoshida, T. Yasuda and Y. Segawa, *Appl. Phys. Lett.*, 1998, **72**, 2466–2468.
- 88 A. K. Sharma, J. Narayan, J. F. Muth, C. W. Teng, C. Jin, A. Kvit, R. M. Kolbas and O. W. Holland, *Appl. Phys. Lett.*, 1999, **75**, 3327–3329.
- 89 T. Makino, Y. Segawa, M. Kawasaki, A. Ohtomo, R. Shiroki, K. Tamura, T. Yasuda and H. Koinuma, *Appl. Phys. Lett.*, 2001, **78**, 1237–1239.
- 90 T. Takagi, H. Tanaka, S. Fujita and S. Fujita, *Jpn. J. Appl. Phys.*, 2003, **42**, L401–L403.
- 91 Y. Nieda, M. Suzuki, A. Nakamura, J. Temmyo, G. Tabares, A. Kurtz, M. Lopez, J. M. Ulloa, A. Hierro and E. Muñoz, *J. Cryst. Growth*, 2016, **449**, 27–34.
- 92 Y. R. Ryu, T. S. Lee, J. A. Lubguban, A. B. Corman, H. W. White, J. H. Leem, M. S. Han, Y. S. Park, C. J. Youn and W. J. Kim, *Appl. Phys. Lett.*, 2006, **88**, 052103.
- 93 M. Toporkov, V. Avrutin, S. Okur, N. Izyumskaya, D. Demchenko, J. Volk, D. J. Smith, H. Morkoç and Ü. Özgür, *J. Cryst. Growth*, 2014, **402**, 60–64.
- 94 J.-H. Lim, C.-K. Kang, K.-K. Kim, I.-K. Park, D.-K. Hwang and S.-J. Park, *Adv. Mater.*, 2006, **18**, 2720–2724.
- 95 D. C. Olson, S. E. Shaheen, M. S. White, W. J. Mitchell, M. F. A. M. van Hest, R. T. Collins and D. S. Ginley, *Adv. Funct. Mater.*, 2007, **17**, 264–269.

- 96 Z. Jin, T. Fukumura, M. Kawasaki, K. Ando, H. Saito, T. Sekiguchi, Y. Z. Yoo, M. Murakami, Y. Matsumoto, T. Hasegawa and H. Koinuma, *Appl. Phys. Lett.*, 2001, **78**, 3824–3826.
- 97 Y. Matsumoto, M. Murakami, T. Shono, T. Hasegawa, T. Fukumura, M. Kawasaki, P. Ahmet, T. Chikyow, S. Koshihara and H. Koinuma, *Science*, 2001, **291**, 854–856.
- 98 T. Fukumura and M. Kawasaki, *Magnetic Oxide Semiconductors: on the High-Temperature Ferromagnetism in TiO₂- and ZnO-Based Compounds* in Ref. 2.
- 99 Y. Yamada, T. Fukumura, K. Ueno and M. Kawasaki, *Appl. Phys. Lett.*, 2011, **99**, 242502.
- 100 Y. Yamada, K. Ueno, T. Fukumura, H. T. Yuan, H. Shimotani, Y. Iwasa, L. Gu, S. Tsukimoto, Y. Ikuhara and M. Kawasaki, *Science*, 2011, **332**, 1065–1067.
- 101 W. Hu, K. Hayashi, T. Fukumura, K. Akagi, M. Tsukada, N. Happpo, S. Hosokawa, K. Ohwada, M. Takahashi, M. Suzuki and M. Kawasaki, *Appl. Phys. Lett.*, 2015, **106**, 222403.
- 102 K. Kaminaga, R. Sei, K. Hayashi, N. Happpo, H. Tajiri, D. Oka, T. Fukumura and T. Hasegawa, *Appl. Phys. Lett.*, 2016, **108**, 122102.
- 103 H. Mizoguchi and H. Hosono, *J. Am. Chem. Soc.*, 2011, **133**, 2394–2397.
- 104 R. Sei, T. Fukumura and T. Hasegawa, *Cryst. Growth Des.*, 2014, **14**, 4227–4229.
- 105 R. Sei, T. Fukumura and T. Hasegawa, *ACS Appl. Mater. Interfaces*, 2015, **7**, 24998–25001.
- 106 R. Sei, S. Kitani, T. Fukumura, H. Kawaji and T. Hasegawa, *J. Am. Chem. Soc.*, 2016, **138**, 11085–11088.
- 107 A. Fuertes, *Inorg. Chem.*, 2006, **45**, 9640–9642.
- 108 D. Oka, Y. Hirose, T. Fukumura and T. Hasegawa, *Cryst. Growth Des.*, 2014, **14**, 87–90.
- 109 D. Oka, Y. Hirose, H. Kamisaka, T. Fukumura, K. Sasa, S. Ishii, H. Matsuzaki, Y. Sato, Y. Ikuhara and T. Hasegawa, *Sci. Rep.*, 2014, **4**, 4987.
- 110 G. Bouilly, T. Yajima, T. Terashima, Y. Kususe, K. Fujita, C. Tassel, T. Yamamoto, K. Tanaka, Y. Kobayashi and H. Kageyama, *CrystEngComm*, 2014, **16**, 9669–9674.
- 111 T. Yajima, A. Kitada, Y. Kobayashi, T. Sakaguchi, G. Bouilly, S. Kasahara, T. Terashima, M. Takano and H. Kageyama, *J. Am. Chem. Soc.*, 2012, **134**, 8782–8785.
- 112 G. Bouilly, T. Yajima, T. Terashima, W. Yoshimune, K. Nakano, C. Tassel, Y. Kususe, K. Fujita, K. Tanaka, T. Yamamoto, Y. Kobayashi and H. Kageyama, *Chem. Mater.*, 2015, **27**, 6354–6359.
- 113 T. Yamamoto, R. Yoshii, G. Bouilly, Y. Kobayashi, K. Fujita, Y. Kususe, Y. Matsushita, K. Tanaka and H. Kageyama, *Inorg. Chem.*, 2015, **54**, 1501–1507.
- 114 T. Katayama, A. Chikamatsu, H. Kamisaka, Y. Yokoyama, Y. Hirata, H. Wadati, T. Fukumura and T. Hasegawa, *AIP Adv.*, 2015, **5**, 107147.
- 115 E. J. Moon, Y. Xie, E. D. Laird, D. J. Keavney, C. Y. Li and S. J. May, *J. Am. Chem. Soc.*, 2014, **136**, 2224–2227.
- 116 R.-J. Xie and H. T. Bert Hintzen, *J. Am. Ceram. Soc.*, 2013, **96**, 665–687.
- 117 Y. Lu, C. Le Paven-Thivet, R. Benzerga, L. Le Gendre, A. Sharaiha, F. Tessier and F. Cheviré, *Appl. Surf. Sci.*, 2013, **264**, 533–537.
- 118 I. Marozau, A. Shkabko, M. Döbeli, T. Lippert, M. Mallepell, C. W. Schneider, A. Weidenkaff and A. Wokaun, *Acta Mater.*, 2011, **59**, 7145–7154.
- 119 Y.-I. Kim, P. M. Woodward, K. Z. Baba-Kishi and C. W. Tai, *Chem. Mater.*, 2004, **16**, 1267–1276.
- 120 A. Ziani, C. Le Paven-Thivet, L. Le Gendre, D. Fasquelle, J. C. Carru, F. Tessier and J. Pinel, *Thin Solid Films*, 2008, **517**, 544–549.
- 121 S. Kikkawa, S. Sun, Y. Masubuchi, Y. Nagamine and T. Shibahara, *Chem. Mater.*, 2016, **28**, 1312–1317.
- 122 A. Suzuki, Y. Hirose, D. Oka, S. Nakao, T. Fukumura, S. Ishii, K. Sasa, H. Matsuzaki and T. Hasegawa, *Chem. Mater.*, 2014, **26**, 976–981.
- 123 J. Takahashi, Y. Hirose, D. Oka, S. Nakao, C. Yang, T. Fukumura, I. Harayama, D. Sekiba and T. Hasegawa, *Appl. Phys. Lett.*, 2015, **107**, 231906.
- 124 T. Yajima, F. Takeiri, K. Aidzu, H. Akamatsu, K. Fujita, W. Yoshimune, M. Ohkura, S. Lei, V. Gopalan, K. Tanaka, C. M. Brown, M. A. Green, T. Yamamoto, Y. Kobayashi and H. Kageyama, *Nat. Chem.*, 2015, **7**, 1017–1023.
- 125 K. J. Choi, *Science*, 2004, **306**, 1005–1009.
- 126 J. H. Haeni, P. Irvin, W. Chang, R. Uecker, P. Reiche, Y. L. Li, S. Choudhury, W. Tian, M. E. Hawley, B. Craigo, A. K. Tagantsev, X. Q. Pan, S. K. Streiffer, L. Q. Chen, S. W. Kirchoefer, J. Levy and D. G. Schlom, *Nature*, 2004, **430**, 758–761.
- 127 N. A. Pertsev, V. G. Kukhar, H. Kohlstedt and R. Waser, *Phys. Rev. B: Condens. Matter Mater. Phys.*, 2003, **67**, 54107.
- 128 R. J. Zeches, M. D. Rossell, J. X. Zhang, A. J. Hatt, Q. He, C.-H. Yang, A. Kumar, C. H. Wang, A. Melville, C. Adamo, G. Sheng, Y.-H. Chu, J. F. Ihlefeld, R. Erni, C. Ederer, V. Gopalan, L. Q. Chen, D. G. Schlom, N. A. Spaldin, L. W. Martin and R. Ramesh, *Science*, 2009, **326**, 977–980.
- 129 A. R. Damodaran, J. C. Agar, S. Pandya, Z. Chen, L. Dedon, R. Xu, B. Apgar, S. Saremi and L. W. Martin, *J. Phys.: Condens. Matter*, 2016, **28**, 263001.
- 130 R. Takahashi, I. Ohkubo, K. Yamauchi, M. Kitamura, Y. Sakurai, M. Oshima, T. Oguchi, Y. Cho and M. Lippmaa, *Phys. Rev. B: Condens. Matter Mater. Phys.*, 2015, **91**, 134107.
- 131 Y. Yun, C. Ma, X. Zhai, H. Huang, D. Meng, J. Wang, Z. Fu, R. Peng, G. J. Brown and Y. Lu, *Appl. Phys. Lett.*, 2015, **107**, 11602.
- 132 Y. Konishi, Z. Fang, M. Izumi, T. Manako, M. Kasai, H. Kuwahara, M. Kawasaki, K. Terakura and Y. Tokura, *J. Phys. Soc. Jpn.*, 1999, **68**, 3790–3793.
- 133 H. W. Yang, H. R. Zhang, Y. Li, S. F. Wang, X. Shen, Q. Q. Lan, S. Meng, R. C. Yu, B. G. Shen and J. R. Sun, *Sci. Rep.*, 2014, **4**, 6206.
- 134 F. Li, C. Song, Y. Y. Wang, B. Cui, H. J. Mao, J. J. Peng, S. N. Li, G. Y. Wang and F. Pan, *Sci. Rep.*, 2015, **5**, 16187.
- 135 L. Marín, L. A. Rodríguez, C. Magén, E. Snoeck, R. Arras, I. Lucas, L. Morellón, P. A. Algarabel, J. M. De Teresa and M. R. Ibarra, *Nano Lett.*, 2015, **15**, 492–497.

- 136 K. Hirai, D. Kan, N. Ichikawa, K. Mibu, Y. Yoda, M. Andreeva and Y. Shimakawa, *Sci. Rep.*, 2015, 5, 7894.
- 137 J. R. Petrie, C. Mitra, H. Jeon, W. S. Choi, T. L. Meyer, F. A. Reboredo, J. W. Freeland, G. Eres and H. N. Lee, *Adv. Funct. Mater.*, 2016, 26, 1564–1570.
- 138 S. Farokhipoor, C. Magén, S. Venkatesan, J. Íñiguez, C. J. M. Daumont, D. Rubi, E. Snoeck, M. Mostovoy, C. de Graaf, A. Müller, M. Döblinger, C. Scheu and B. Noheda, *Nature*, 2014, 515, 379–383.
- 139 T. Ohnishi, M. Lippmaa, T. Yamamoto, S. Meguro and H. Koinuma, *Appl. Phys. Lett.*, 2005, 87, 241919.
- 140 S. A. Lee, H. Jeong, S. Woo, J.-Y. Hwang, S.-Y. Choi, S.-D. Kim, M. Choi, S. Roh, H. Yu, J. Hwang, S. W. Kim and W. S. Choi, *Sci. Rep.*, 2016, 6, 23649.
- 141 A. Sarantopoulos, E. Ferreiro-Vila, V. Pardo, C. Magén, M. H. Aguirre and F. Rivadulla, *Phys. Rev. Lett.*, 2015, 115, 166801.
- 142 A. R. Damodaran, E. Breckenfeld, Z. Chen, S. Lee and L. W. Martin, *Adv. Mater.*, 2014, 26, 6341–6347.
- 143 Y. Kim, A. N. Morozovska, A. Kumar, S. Jesse, E. A. Eliseev, F. Alibart, D. Strukov and S. V. Kalinin, *ACS Nano*, 2012, 6, 7026–7033.
- 144 A. S. Borowiak, N. Baboux, D. Albertini, B. Vilquin, G. Saint Girons, S. Pelloquin and B. Gautier, *Appl. Phys. Lett.*, 2014, 105, 12906.
- 145 P. Sharma, S. Ryu, Z. Viskadourakis, T. R. Paudel, H. Lee, C. Panagopoulos, E. Y. Tsymlal, C.-B. Eom and A. Gruverman, *Adv. Funct. Mater.*, 2015, 25, 6538–6544.
- 146 J. He, A. Borisevich, S. V. Kalinin, S. J. Pennycook and S. T. Pantelides, *Phys. Rev. Lett.*, 2010, 105, 227203.
- 147 J. M. Rondinelli and N. A. Spaldin, *Phys. Rev. B: Condens. Matter Mater. Phys.*, 2010, 82, 113402.
- 148 A. Y. Borisevich, H. J. Chang, M. Huijben, M. P. Oxley, S. Okamoto, M. K. Niranjani, J. D. Burton, E. Y. Tsymlal, Y. H. Chu, P. Yu, R. Ramesh, S. V. Kalinin and S. J. Pennycook, *Phys. Rev. Lett.*, 2010, 105, 087204.
- 149 J. M. Rondinelli, S. J. May and J. W. Freeland, *MRS Bull.*, 2012, 37, 261–270.
- 150 R. Aso, D. Kan, Y. Shimakawa and H. Kurata, *Sci. Rep.*, 2013, 3, 2214.
- 151 R. Aso, D. Kan, Y. Shimakawa and H. Kurata, *Adv. Funct. Mater.*, 2014, 24, 5177–5184.
- 152 D. Kan, R. Aso, R. Sato, M. Haruta, H. Kurata and Y. Shimakawa, *Nat. Mater.*, 2016, 15, 432–437.
- 153 D. Kan, R. Aso, H. Kurata and Y. Shimakawa, *Dalton Trans.*, 2015, 44, 10594–10607.
- 154 Z. Liao, M. Huijben, Z. Zhong, N. Gauquelin, S. Macke, R. J. Green, S. Van Aert, J. Verbeeck, G. Van Tendeloo, K. Held, G. A. Sawatzky, G. Koster and G. Rijnders, *Nat. Mater.*, 2016, 15, 425–431.
- 155 L. Qiao, J. H. Jang, D. J. Singh, Z. Gai, H. Xiao, A. Mehta, R. K. Vasudevan, A. Tselev, Z. Feng, H. Zhou, S. Li, W. Prellier, X. Zu, Z. Liu, A. Borisevich, A. P. Baddorf and M. D. Biegalski, *Nano Lett.*, 2015, 15, 4677–4684.
- 156 H. Chen, Q. Qiao, M. S. J. Marshall, A. B. Georgescu, A. Gulec, P. J. Phillips, R. F. Klie, F. J. Walker, C. H. Ahn and S. Ismail-Beigi, *Nano Lett.*, 2014, 14, 4965–4970.
- 157 D. Preziosi, M. Alexe, D. Hesse and M. Salluzzo, *Phys. Rev. Lett.*, 2015, 115, 157401.
- 158 A. Evans, A. Bieberle-Hütter, J. L. M. Rupp and L. J. Gauckler, *J. Power Sources*, 2009, 194, 119–129.
- 159 A. Orera and P. R. Slater, *Chem. Mater.*, 2010, 22, 675–690.
- 160 M. Park, X. Zhang, M. Chung, G. B. Less and A. M. Sastry, *J. Power Sources*, 2010, 195, 7904–7929.
- 161 S. Shiraki, H. Oki, Y. Takagi, T. Suzuki, A. Kumatani, R. Shimizu, M. Haruta, T. Ohsawa, Y. Sato, Y. Ikuhara and T. Hitosugi, *J. Power Sources*, 2014, 267, 881–887.
- 162 A. Ohtomo and H. Hwang, *Nature*, 2004, 427, 423–425.
- 163 A. Tsukazaki, A. Ohtomo, T. Kita, Y. Ohno, H. Ohno and M. Kawasaki, *Science*, 2007, 315, 1388–1391.
- 164 D. A. Dikin, M. Mehta, C. W. Bark, C. M. Folkman, C. B. Eom and V. Chandrasekhar, *Phys. Rev. Lett.*, 2011, 107, 56802.
- 165 S. Thiel, *Science*, 2006, 313, 1942–1945.
- 166 N. Reyren, S. Thiel, A. D. Caviglia, L. F. Kourkoutis, G. Hammerl, C. Richter, C. W. Schneider, T. Kopp, A.-S. Ruetschi, D. Jaccard, M. Gabay, D. A. Muller, J.-M. Triscone and J. Mannhart, *Science*, 2007, 317, 1196–1199.
- 167 X. Wan, A. M. Turner, A. Vishwanath and S. Y. Savrasov, *Phys. Rev. B: Condens. Matter Mater. Phys.*, 2011, 83, 205101.
- 168 M. Bibes, J. E. Villegas and A. Barthélémy, *Adv. Phys.*, 2011, 60, 5–84.
- 169 D. W. Jeong, W. S. Choi, S. Okamoto, J. Kim, K. W. Kim, S. J. Moon, D. Cho, H. N. Lee and T. W. Noh, *Sci. Rep.*, 2014, 4, 6124.
- 170 A. K. Yadav, C. T. Nelson, S. L. Hsu, Z. Hong, J. D. Clarkson, C. M. Schlepütz, A. R. Damodaran, P. Shafer, E. Arenholz, L. R. Dedon, D. Chen, A. Vishwanath, A. M. Minor, L. Q. Chen, J. F. Scott, L. W. Martin and R. Ramesh, *Nature*, 2016, 530, 198–201.
- 171 N. Doiron-Leyraud, C. Proust, D. LeBoeuf, J. Levallois, J.-B. Bonnemaison, R. Liang, D. A. Bonn, W. N. Hardy and L. Taillefer, *Nature*, 2007, 447, 565–568.
- 172 B. J. Kim, H. Ohsumi, T. Komesu, S. Sakai, T. Morita, H. Takagi and T. Arima, *Science*, 2009, 323, 1329–1332.
- 173 S. Fujiyama, H. Ohsumi, T. Komesu, J. Matsuno, B. J. Kim, M. Takata, T. Arima and H. Takagi, *Phys. Rev. Lett.*, 2012, 108, 247212.
- 174 L. Mazet, S. M. Yang, S. V. Kalinin, S. Schamm-Chardon and C. Dubourdieu, *Sci. Technol. Adv. Mater.*, 2015, 16, 36005.
- 175 M. Nijland, S. Thomas, M. A. Smithers, N. Banerjee, D. H. A. Blank, G. Rijnders, J. Xia, G. Koster and J. E. ten Elshof, *Adv. Funct. Mater.*, 2015, 25, 5140–5148.
- 176 T. Yoshida, J. Zhang, D. Komatsu, S. Sawatani, H. Minoura, T. Pauporté, D. Lincot, T. Oekermann, D. Schlettwein, H. Tada, D. Wöhrle, K. Funabiki, M. Matsui, H. Miura and H. Yanagi, *Adv. Funct. Mater.*, 2009, 19, 17–43.
- 177 J.-P. Niemelä, A. J. Karttunen and M. Karppinen, *J. Mater. Chem. C*, 2015, 3, 10349–10361.